



Investigation of heat source modeling for selective laser melting

H. Wessels¹ · T. Bode¹ · C. Weißenfels¹ · P. Wriggers¹ · T. I. Zohdi²

Received: 1 May 2018 / Accepted: 26 August 2018
© Springer-Verlag GmbH Germany, part of Springer Nature 2018

Abstract

Selective Laser Melting (SLM) is an emerging Additive Manufacturing technology for metals. Complex three dimensional parts can be generated from a powder bed by locally melting the desired portions layer by layer. The necessary heat is provided by a laser. The laser–matter interaction is a crucial physical phenomenon in the SLM process. Various modeling approaches with different degrees of complexity exist in the literature to represent the laser–matter interaction within a numerical framework. Often, the laser energy is simply distributed into a specified volume. A more precise approach is ray tracing. The laser beam can be divided into moving discrete energy portions (rays) that are traced in space and time. In order to compute the reflection and absorption usually a triangulation of the free surface is conducted. Within meshfree methods, this is a very expensive operation. In this work, a computationally efficient algorithm is developed which avoids triangulation and can easily be combined with meshfree methods. Here, the suggested ray tracing algorithm is exemplary coupled with the stabilized Optimal Transportation Meshfree Method. The importance of ray tracing is evaluated by simulating the fusion of metal powder particles. A comparison of the results with a volumetric heat source approach shows that ray tracing significantly improves the accuracy of absorption and vaporization.

Keywords Additive manufacturing · Selective laser melting · Ray tracing · Optimal Transportation Meshfree method

1 Introduction

In Selective Laser Melting, metal parts are built up from a powder bed layer by layer. A laser locally melts the powder bed. The initial high volume to surface ratio of powdered material makes surface tension the most important driving force for the process. Other phenomena related to surface tension are Marangoni convection, the balling effect and the wetting of solid material with melt. Escaping vapor in the rear of the laser beam may indent the melt pool if the energy input is high. This is called keyholing. During consolidation, inhibited thermal expansion and the change of material stiffness initiate residual stresses. The fast thermal cycles result in an AM-specific micro-structure that determines the mechanical properties. The physical phenomena are schematically illustrated in Fig. 1. A detailed review on laser based AM of

metallic components, the involved physical phenomena and their influence on the micro-structure can be found in [14].

The SLM process offers a unique geometrical flexibility for designers to create innovative parts. The flexibility of SLM could be further increased to a structural level: Ideally, one could alter process parameters in order to locally manipulate the micro-structure and customize parts to individual performance requirements. Such a detailed process planning is prohibitively expensive with conventional, experience driven approaches. Computational simulation techniques promise to save time and resources. When modeling at powder scale, the free surface evolution and surface tension effects are the key challenges to predict the SLM process. The problem has been tackled with a variety of numerical tools such as Finite Volumes (FV), the Lattice-Boltzmann (LBM) and the Arbitrary Lagrangian Eulerian (ALE) method, see [1,34] and [20]. A common drawback of LBM, ALE and FV is the need for special numerical treatments such as e.g. the Volume of Fluid (VoF) approach to resolve the free surface and surface tension effects. This becomes especially pronounced when modeling the fusion of metal powder particles.

✉ H. Wessels
wessels@ikm.uni-hannover.de

¹ Institute of Continuum Mechanics, Leibniz University of Hannover, Appelstr. 11, 30167 Hannover, Germany

² Department of Mechanical Engineering, 6117 Etcheverry Hall, University of California, Berkeley, CA 94720-1740, USA

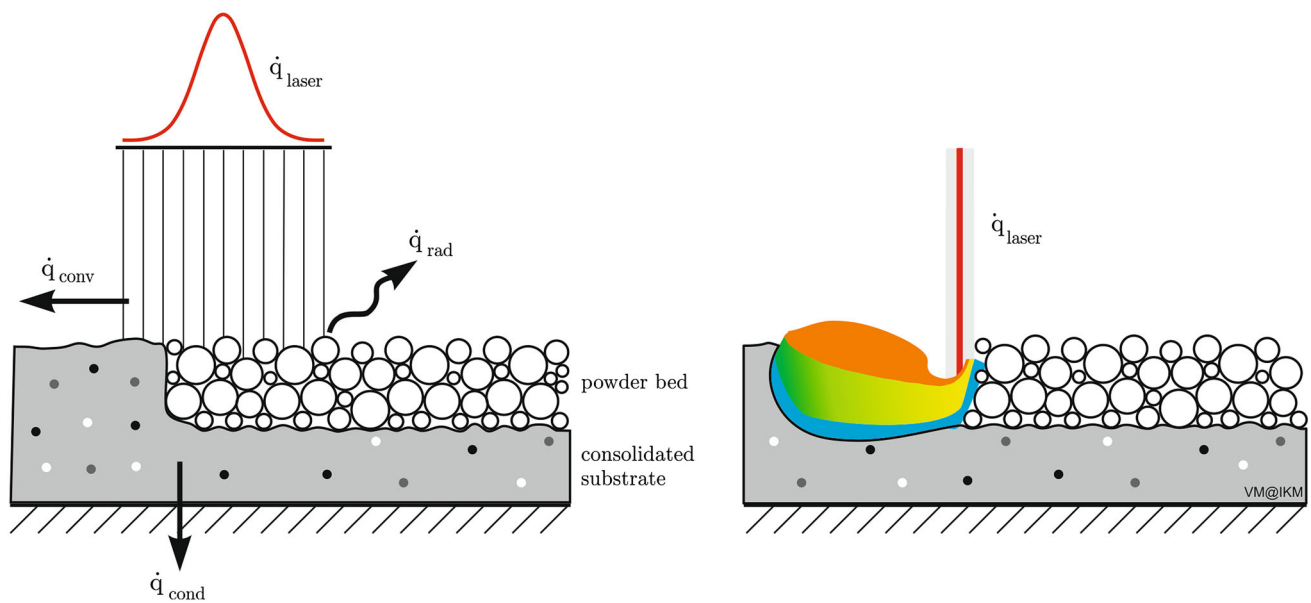


Fig. 1 Left: the incident laser irradiation \dot{q}_{laser} is emitted by thermal conduction \dot{q}_{cond} , convection \dot{q}_{conv} and radiation \dot{q}_{rad} . Right: escaping vapor indents the melt pool. Grey colored dots are vaporized, black dots non-molten powder particles and white dots surrounding gas. (Color figure online)

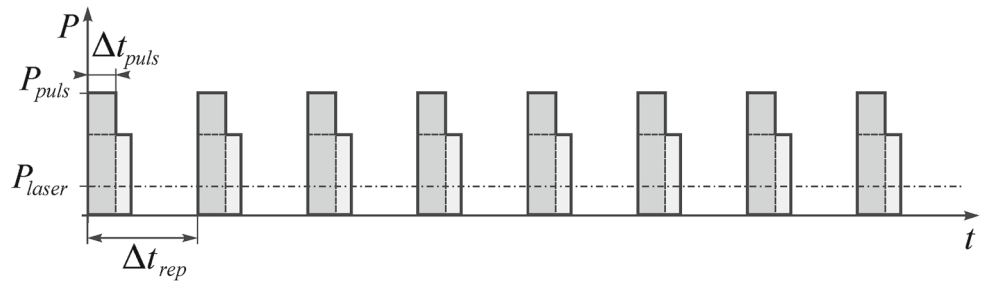
In Lagrangian meshfree and particle methods the tracking of the free surface is intrinsic. Particle deposition with subsequent as well as on-the-fly laser processing has been investigated with the Discrete Element Method (DEM) in [39] and [45], respectively. Ganeriwala and Zohdi [9] developed a DEM framework to simulate a single laser track of the SLM process. Due to the discrete nature of the DEM method, the model accounts for the statistical nature of the powder bed but lacks a physical representation of the melt flow. One way to overcome this drawback is the use of hybrid DEM-continuum approaches, see e.g. [42]. Here, a continuum meshfree scheme is employed. Recently, Wessels et al. [30] have developed a thermo-mechanical phase change model accounting for finite deformations. The model has been implemented into the stabilized Optimal Transportation Meshfree (OTM) framework. It has been shown that the proposed methodology is feasible to investigate the influence of laser power and heat transfer on the fusion of metal powder particles. This work concentrates on the heat source modeling in meshfree powder scale SLM simulations.

Zohdi [39] names four stages of sophistication to model the laser input: First, neglecting thermal conduction, the heating $\Delta\theta$ can be estimated from the energy absorbed by the powder bed. This assumption is clearly not accurate enough on the powder scale of SLM processes. For part scale simulations however, the superposition of heat-kernel solutions as suggested in [44] can be employed as a computationally efficient heat source. The next step of sophistication is to assume a volumetric intensity distribution. Another approach is ray tracing, where the beam is discretized into energy portions, so-called rays. The last step of sophistica-

tion is to represent the beam by its electro-magnetic field components via Maxwell equations. While this formulation provides a high level of accuracy, see [37], it also comes at a high computational cost and is not feasible within a particle melting simulation. Oftentimes, volumetric heat sources are used because of their ease of implementation. However, their motivation is mostly based on empirical observations. Also, the absorption highly depends on the overlap of the volumetric intensity distribution with the irradiated geometry. This is a severe concern in powder scale SLM simulations. For an accurate description of absorption and reflection, ray tracing is most appropriate. It is a purely geometrical approach and applicable if diffraction is not expected to occur. In SLM, this is fulfilled since the diameter of powder particles and the characteristic surface features are more than an order of magnitude larger than the wavelength of the incident radiation.

Ray tracing is commonly used in optics, see e.g. [13,35] and [46]. The scattering of incident radiation in particulate media has been investigated in [36,40], and [43], for instance. Also in metal processing simulations ray tracing is a useful numerical tool. Zohdi [38] developed a ray tracing algorithm for DEM to investigate the laser-matter interaction of irradiated powdered material. Ki et al. [22] established a detailed model for laser keyhole welding for solution with the mesh-based Finite Difference Method. Therein the evolution of the liquid-vapor interface is tracked with a level set method. At the same time, the level sets provide the surface normals for the coupling with a ray tracing algorithm. Hu and Eberhard [17] used ray tracing to determine the absorptivity of metal during conduction mode laser welding. The absorptivity of

Fig. 2 Sequence of rectangular laser pulses. Illustration of pulsing width Δt_{puls} , repetition rate $f_{rep} = 1/\Delta t_{rep}$, pulsing power P_{puls} and effective laser power P_{laser}



solid and liquid metal is then fed into a Smoothed Particle Hydrodynamics (SPH) simulation, where a volumetric heat source is employed. In subsequent work, Hu et al. [18] have developed a coupling algorithm for ray tracing and SPH. To compute the reflection, a triangulation of the free surface was conducted.

The triangulation is a computationally very expensive operation. Here, a coupling algorithm for ray tracing and meshfree solution schemes is developed that overcomes the necessity of a surface triangulation. The proposed methodology is exemplary applied to the stabilized OTM method. The outline of this work is as follows: Sect. 2 gives an overview of heat source modeling. The thermo-mechanical model is briefly summarized in Sect. 3. The explicit and implicit stabilized OTM solution schemes employed in this work are presented in Sect. 4. The coupling algorithm for ray tracing and OTM is established in Sect. 5. In a particle melting analysis, volumetric heat source modeling and ray tracing are compared to each other (see Sect. 6). The paper concludes with a summary and an outlook in Sect. 7.

2 Heat source modeling

Lasers can emit power in pulses and in special cases continuously. Both pulsing and continuous laser beams will be considered in this work. A rectangular laser pulse is defined by the pulse width Δt_{pulse} , the repetition rate f_{rep} and the pulsing power P_{pulse} . The effective (continuous) laser power P_{laser} can be computed from:

$$P_{laser} = f_{rep} \Delta t_{pulse} P_{pulse} \tag{1}$$

In a pulsed laser the currently emitted power P is a function of time t . As graphically illustrated in Fig. 2, a sequence of n_{pulse} rectangular pulses can be expressed by a series of Heaviside functions:

$$P(t) = P_{pulse} \sum_{n=0}^{n_{pulse}} \left[H_n \left(t - \frac{n}{f_{rep}} \right) - H_n \left(t - \frac{n}{f_{rep}} - \Delta t_{pulse} \right) \right] \tag{2}$$

In ray tracing and volumetric heat source modeling the emission of laser energy is expressed by an intensity function. For a circular focused beam, a radial intensity distribution $I_{rad}(r)$ is most appropriate. It distributes the power $P(t)$ within an area da :

$$P(t, r) = P(t) I_{rad}(r) \quad \text{with} \quad \int_0^\infty I_{rad}(r) da = 1 \tag{3}$$

Here the variable r is the radial distance from the laser’s focal midpoint. Oftentimes a Gaussian distribution is assumed, where the standard deviation is half the beam radius R :

$$I_{rad}(r) = \frac{2}{\pi R^2} e^{-2r^2/R^2} \tag{4}$$

The laser beam radius R can be defined as the radius where the intensity reduces to $1/e^2$ of the peak intensity. This corresponds to 86.47% of the laser power that is focused in the circular laser spot. In this work, the Gaussian distribution is normalized in order to distribute the entire laser power within the spot:

$$I_{rad}(r) = \frac{2}{\pi R^2 (1 - e^{-2})} e^{-2r^2/R^2} \tag{5}$$

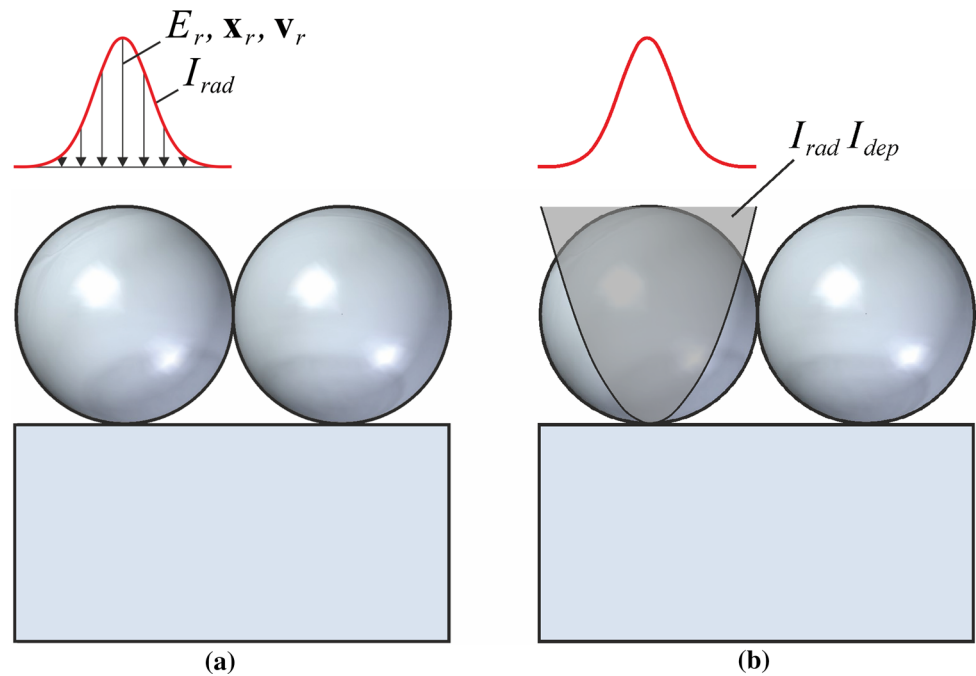
An introduction to laser technology and an overview of related intensity distributions for various laser applications can be found for instance in [16].

2.1 Ray tracing

The theory of ray tracing can be motivated from Maxwell’s equations, see e.g. [38]. Ray tracing can also be regarded as a spatial and temporal discretization of a heat source into discrete energy portions (rays). A planar wavefront is represented by collinear rays that are emitted at specified time steps. Initially, the rays are placed at random positions inside the laser spot. This is sketched in Fig. 3a. The amount of energy E_r assigned to a ray depends on its position \mathbf{x}_r within the beam:

$$E_r = \Delta t_r P(t) w_r(r_r) \tag{6}$$

Fig. 3 Heat source modeling. **a** Using ray tracing the laser is divided into discrete energy portions (rays) that are absorbed by the irradiated part. **b** With a volumetric heat source model, most of the laser power is distributed into the grey shaded volume



The time increment of ray creation is denoted Δt_r . The weight w_r is a function of the radial distance r_r of a ray to the laser's focal midpoint. It is obtained by normalization of the radial intensity distribution:

$$w_r = \frac{I_{rad}(r_r)}{\sum_q^{n_{rpl}} I_{rad}(r_q)} \quad (7)$$

Here n_{rpl} is the number of rays per level, i.e. the number of rays that are created within a time step Δt_r . In this work, a Gaussian beam is used with I_{rad} defined as in (5). The rays propagate in time at constant velocity \mathbf{v}_r . The actual ray velocity depends on the permittivity and permeability in free space as well as on the medium the rays are traversing. It is in the order of the speed of light in Argon gas, i.e. $\approx 3 \times 10^8$ m/s. To resolve the conflict of scales between the thermal problem and the ray propagation, the ray velocity is scaled by a factor k^{red} . The ray positions \mathbf{x}_r are updated in each time step Δt of the discrete thermal problem:

$$\mathbf{x}_{r\ n+1} = \mathbf{x}_{r\ n} + k^{red} \mathbf{v}_r \Delta t \quad (8)$$

The coupling between the ray tracing algorithm and OTM as well as the scaling factor k^{red} are discussed in Sect. 5.

2.2 Volumetric heat sources

The idea of volumetric heating terms is to distribute the incident power into a specified volume. It is most appropriate if the heat source can disperse into the irradiated

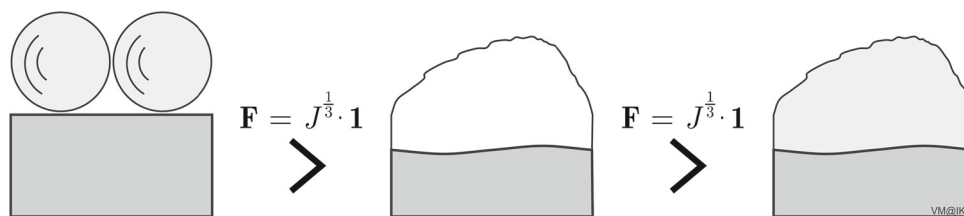
system. The shape of the function that describes the irradiated volume is based on theoretical considerations or empirical observations. Many formulations of volumetric heating terms have been developed for various applications. Goldak et al. [10] suggested a double ellipsoidal model which is widely used by the welding community. The idea is to distribute the absorbed energy into the weld pool, whose geometry has to be estimated from experiments. Yan et al. [33] use a Monte Carlo method to model electron penetration into a metal powder bed. The outcome is a physically informed volumetric heat source for the Electron Beam Melting (EBM) process, see [34]. Based on an analytical solution of the radiation transfer equation, Gusarov et al. [15] established a volumetric heat source for the SLM process which accounts for the multiple reflections inside the powder bed. Ganeriwala and Zohdi [9] use a volumetric heat source based on a Beer–Lambert equation to model the powder bed irradiation. Generally, a volumetric intensity distribution consists of a radial component I_{rad} and a contribution I_{dep} that describes the penetration of the laser into the part:

$$P(t, r, z) = P(t) I_{rad}(r) I_{dep}(z) \quad (9)$$

$$\text{with } \int_0^L \int_0^\infty I_{rad}(r) I_{dep}(z) da dz = 1$$

Here L is the maximum penetration depth of the heat source. The concept is graphically illustrated in Fig. 3b. The Gusarov-type heat source and the Beer–Lambert law are summarized in the subsequent sections.

Fig. 4 When a phase change occurs, the deviatoric deformation gradient \mathbf{F}_{dev} is set equal to one. Only the volumetric part \mathbf{F}_{vol} remains. Left: Powder Particles. Centered: Molten metal. Right: consolidated metal



2.2.1 Gusarov type heat source

Gusarov et al. [15] assume a bell-like radial intensity function:

$$I_{rad}(r) = \frac{3}{\pi R^2} \left(1 - \frac{r}{R}\right)^2 \left(1 + \frac{r}{R}\right)^2 \quad (10)$$

The dependence of the intensity on the powder bed penetration depth z is modeled as:

$$I_{dep}(z) = -\beta(r) \frac{dq}{d\xi(z)} \quad \text{with} \quad \beta = \frac{3(1 - \varepsilon_b)}{2 \varepsilon_b D} = \frac{\lambda}{L} \quad (11)$$

Here q denotes the dimensionless laser energy density and $\xi(z) = \beta z$ a dimensionless coordinate. The optical extinction coefficient β takes into account the powder bed porosity ε_b and the particle diameter D . It can also be obtained from the optical thickness λ and the powder bed depth L , see [15] for details. The differentiation of q with respect to $\xi(z)$ can be found in [30].

2.2.2 Beer–Lambert

The Beer–Lambert law assumes an exponential decrease of absorptivity with penetration depth:

$$I_{dep}(z) = I_{0z} e^{-\int_0^z \beta(z) dz} \quad (12)$$

For a porous metal powder bed, the extinction coefficient β can be taken as a constant value as defined in the theory of [15]. The coefficient I_{0z} is obtained from normalization of the intensity function over the powder bed depth L . The normalized Beer–Lambert law for the powder bed yields:

$$I_{dep}(z) = \beta \left(1 - e^{-\beta L}\right)^{-1} e^{-\beta z} \quad (13)$$

Due to the normalization, losses with respect to penetration depth are not accounted for in this formulation.

3 Thermo-mechanical modeling

In the last decades the interest in metal phase change modeling mainly focused on welding and casting applications.

In both processes deformations are small and an additive split of strains is sufficient, see e.g. [11]. However, on the powder scale of SLM the liquid melt flow has to be taken into account and the strains are finite. Recently, in [30] a thermo-mechanical phase change model has been developed that is applicable in the finite deformation regime. It has been demonstrated that this concept is suitable to represent the main physical effects occurring on the powder scale of SLM processes. The deformation gradient \mathbf{F} is multiplicatively split into a volumetric and a deviatoric part. The underlying assumption is that only the deviatoric deformation gradient \mathbf{F}_{dev} has a fading memory due to the phase change:

$$\mathbf{F}_{dev} = \mathbf{1} \quad \mathbf{F} = \mathbf{F}_{vol} = J^{\frac{1}{3}} \mathbf{1} \quad (14)$$

The volumetric deformation gradient \mathbf{F}_{vol} is mainly caused by thermal expansion and preserved throughout all phases, see also Fig. 4. Following the concept of Lu and Pister [24], a decomposed free energy function for the finite deformation phase change problem has been postulated in [30]. Differentiation of the free energy function yields the entropy work and the stress tensor. These quantities are necessary to properly define the governing energy and momentum equations. For further details on the theoretical background, the reader is referred to the original publication. The resulting equations are briefly summarized in the following sections.

3.1 Energy equation

When modeling the SLM process, several assumptions can be made on the first law of thermodynamics: First, dissipation is neglected. In the solid phase, this is the consequence of assuming that the material behaves elastically. This assumption is a severe limitation of the model but it can be completed by including visco-plastic contributions. A viscous heating term has also not been taken into account since liquid melt is nearly inviscid. Second, since volumetric deformation is mostly related to thermal expansion, heating caused by elastic volumetric deformation is neglected. The heat flux is of Fourier type with isotropic conductivity k . Implementing these considerations, the energy equation can be written as:

$$\rho(c + L_\theta) \dot{\theta} = k \operatorname{div}(\operatorname{grad} \theta) \quad (15)$$

Here ρ is the density, c the heat capacity, θ the temperature, $\dot{\theta}$ its rate and r^s a volumetric heating term. The treatment of the latent heat contribution L_θ employed in (15) is analogous to the apparent heat capacity method introduced by Bonacina et al. [4] and recently studied by Muhieddine et al. [25]. It is most appropriate for materials that change phase over a temperature range between a solidus (bubble) and a liquidus (dew) temperature T_{sol} (T_{bubble}) and T_{liq} (T_{dew}). The latent heat is absorbed in this temperature interval. In this work, the apparent heat capacity method is used to facilitate the coupling of energy and momentum equation.

When a volumetric heat source is employed, the heating is obtained from $\rho r^s = P(t) I(r, z)$. The coupling of energy equation and ray tracing scheme is discussed in Sect. 5.

Boundary fluxes related to convection and radiation can be imposed as discussed e.g. in [30]. However, since Ganeriwala and Zohdi [9] have pointed out that heat conduction outnumbers these effects by several orders of magnitude they have been neglected in the present analysis.

3.2 Momentum equation

The stress tensor is decomposed into a hydrostatic part defined by the pressure p and into a phase dependent deviatoric tensor \mathbf{s} . The equation of motion is given by

$$\rho \mathbf{a} = -\text{grad } p + \text{div } \mathbf{s}(\phi) + \rho \hat{\mathbf{b}} \quad (16)$$

where ϕ is the phase variable, \mathbf{a} the material and $\hat{\mathbf{b}}$ the gravitational acceleration. The pressure p is calculated from the constitutive equation for a compressible material:

$$-p = \frac{K}{J} \ln J_e \quad \text{with} \quad J_e = J e^{-3\alpha_\theta(\theta - \theta_0)} \quad (17)$$

Here K is the compression modulus, J_e the elastic Jacobi determinant, α_θ the thermal expansion coefficient and θ_0 a reference temperature. The deviatoric stress model switches from an elastic spring in the solid phase to a viscous damper in the liquid phase and vice versa. In the solid phase ($\phi = 1$) the deviatoric stress is defined with the second Lamé constant μ as:

$$\mathbf{s}(\phi = 1) = \frac{\mu}{J} \left(\bar{\mathbf{b}} - \frac{1}{3} (\text{tr } \bar{\mathbf{b}}) \mathbf{1} \right) \quad \text{with} \quad \bar{\mathbf{b}} = J^{-\frac{2}{3}} \mathbf{b} \quad (18)$$

Here $\mathbf{b} = \mathbf{F}\mathbf{F}^T$ is the left Cauchy Green tensor and $\bar{\mathbf{b}}$ its isochoric counterpart. In the liquid phase ($\phi = 0$), viscous stresses are defined from

$$\mathbf{s}(\phi = 0) = \frac{2\eta}{J} \left(\mathbf{d} - \frac{1}{3} (\text{tr } \mathbf{d}) \cdot \mathbf{1} \right) \quad (19)$$

where η is the dynamic viscosity. Therein, the tensor \mathbf{d} is the symmetric part of the spatial velocity gradient. In SLM, the difference between cohesive forces of liquid metal and surrounding Argon gas results in a surface tension \mathbf{t} . It is imposed to the problem as a Neumann boundary condition $\mathbf{t}^{surf} = \boldsymbol{\sigma} \cdot \mathbf{n}$ with

$$\mathbf{t}^{surf} = \gamma \kappa \mathbf{n} \quad (20)$$

Here \mathbf{n} is the surface normal and κ the curvature of the interface between melt and surrounding Argon gas. The surface tension coefficient γ is in general a function of temperature which yields the aforementioned Marangoni effect.

To avoid the simulation of the gas phase, its interaction with the liquid metal can be represented by a recoil pressure. It can again be incorporated into the suggested continuum model as a Neumann boundary condition from a relation found by Anisimov and Khokhlov [2] which was e.g. used in the work of Khairallah et al. [21]:

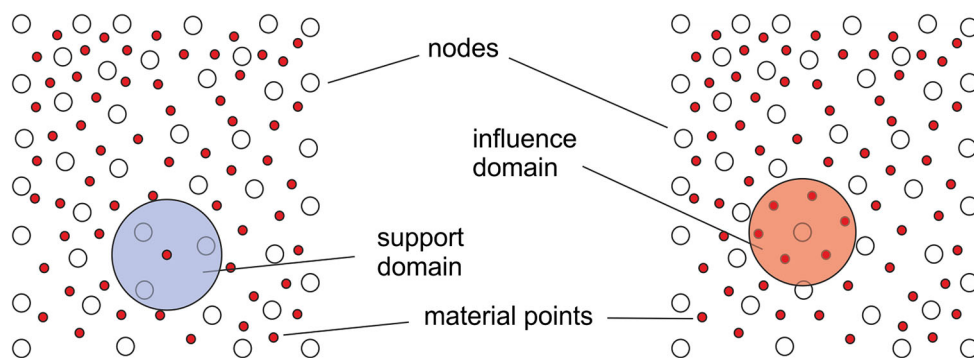
$$\mathbf{t}^{rec} = p^{rec}(\theta) \mathbf{1} \quad \text{with} \quad p^{rec}(\theta) = 0.54 p_a \exp \left(\frac{\lambda}{k_b} \left(\frac{1}{\theta} - \frac{1}{T_{vap}} \right) \right) \quad (21)$$

Here p_a is the ambient pressure, λ the evaporation energy per atom, k_b the Boltzmann constant and T_{vap} the vaporization temperature. Since the recoil pressure expands the liquid-vapor interface, it counteracts surface tension which tends to minimize it. In the present study, Marangoni effect and recoil pressure have been neglected.

4 Stabilized optimal transportation meshfree method

The OTM method is an Updated Lagrangian scheme that has initially been introduced by Li et al. [23]. In the original publication a nodal rearrangement is necessary in every time step in order to equilibrate configurational forces. Weißenfels and Wriggers [29] suggested a stabilized OTM that overcomes the necessity of a shifting algorithm. This approach is applied in the current analysis. In the OTM framework, the primary variables and their time derivatives are nodal quantities, whereby mass, volume, density and stress are defined at the material points. During the computation a search algorithm establishes the connectivity between material points and nodes. All nodes connected to a material point form its support domain. The material point coordinate \mathbf{x}_p is interpolated from the positions \mathbf{x}_I of nodes inside the support domain with the aid of shape functions N_I :

Fig. 5 Spatial discretization with the Optimal Transportation Meshfree method



$$\mathbf{x}_p = \sum_p^{N_p^{sup}} N_I(\mathbf{x}_p) \mathbf{x}_I \tag{22}$$

Here N_p^{sup} denotes the number of nodes inside a support domain. The spatial discretization into nodes and material points is schematically illustrated in Fig. 5. The number of nodes per support domain is in general arbitrary. This necessitates the use of special shape functions. Li et al. [23] suggest Local Maximum Entropy (LME) shape functions introduced by Arroyo and Ortiz [3] within the OTM framework.

In both the original OTM of Li et al. [23] and the stabilized approach of Weïßenfels and Wriggers [29] explicit time integration is employed. For application in laser based Additive Manufacturing, Wessels et al. [30] have recently introduced an implicit stabilized OTM algorithm. In this work, in order to establish the coupled ray tracing OTM approach an explicit purely thermal code is employed. Since the Courant–Friedrichs–Lewy (CFL) condition in explicit schemes is very restrictive for the mechanical problem, the implicit time integration is preferred in the particle fusion analysis.

The outline of this section is as follows: First, the energy equation for solution with the explicit OTM scheme is presented. The implicit algorithm introduced in [30] is summarized in Sect. 4.2. The spatial discretization with a search algorithm and LME shape functions is discussed in Sect. 4.3.

4.1 Explicit solution of the energy equation with OTM

Weïßenfels and Wriggers [29] have shown that the OTM can be derived from the principle of virtual work. Hence, the weak form of the energy equation is obtained by multiplying the strong form (15) with a trial function $\delta\theta$. After partially integrating and neglecting surface boundary heat fluxes it can be expressed as:

$$\int_v \rho (c + L_\theta) \dot{\theta} \delta\theta \, dv + \int_v k \text{grad } \theta \text{ grad } \delta\theta \, dv - \int_v \delta\theta \rho r^s \, dv = 0 \tag{23}$$

Here dv is the volume element. Following the standard Bubnov–Galerkin approximation, the same shape functions are employed to interpolate the primary variable and the trial function. This leads to the spatially discretized heat equation:

$$\mathbf{C} \dot{\boldsymbol{\theta}}_n + \mathbf{K} \boldsymbol{\theta}_n - \mathbf{Q} = \mathbf{0} \tag{24}$$

The discrete equations are assembled within loops over all material points n_{mp} and their support domains of size N_{pn}^{sup} at the time step n . The heat capacity and the thermal conductivity matrices can be found in the appendix in (54). The discretization of the heat input vector \mathbf{Q} depends on the type of heat source model used. It can be written in general form:

$$\mathbf{Q} = \bigcup_{p=1}^{n_{mp}} \sum_{I=1}^{N_{pn}^{sup}} N_I(\mathbf{x}_{pn}) P_{pn} \tag{25}$$

The coupling of OTM and ray tracing will be discussed later on in this work. When the volumetric heating term is used, the power P_{pn} follows the discrete form of (9) with the radial distance r_{pn} and penetration depth z_{pn} :

$$P_{pn} = \rho_{pn} r_{pn}^s v_{pn} = P(t_n) I(r_{pn}, z_{pn}) v_{pn} \tag{26}$$

For the temporal discretization the forward Euler scheme is employed. In combination with the lumped heat capacitance matrix the nodal temperatures can be computed explicitly. At every node (except at Dirichlet boundaries) the temperature is updated from:

$$\theta_{I_{n+1}} = \sum_p^{N_{In}^{inf}} \sum_J^{N_{pn}^{sup}} \left(\theta_{I_n} - \frac{\Delta t}{m_{In}} \frac{k_{pn}}{c_{pn}} v_{pn} \frac{N_I(\mathbf{x}_{pn})}{\partial \mathbf{x}_{pn}} \frac{N_J(\mathbf{x}_{pn})}{\partial \mathbf{x}_{pn}} \theta_{I_n} + \Delta t P_{pn} \right) \tag{27}$$

The nodal mass m_{In} is interpolated from the N_I^{inf} material point masses m_p inside the influence domain of a node.

Fried and Rheinboldt [8] have shown that for the choice of the time step increment within an explicit scheme stability concerns override those of accuracy. They suggest the following criterion to ensure stability and convergence:

$$\Delta t \leq C \frac{\rho c}{k} h^2 \quad 0 < C < 1 \tag{28}$$

Here h is a typical length that can be chosen as the third root of material point volume in three dimensional computations.

4.2 Implicit thermo-mechanical stabilized OTM

The strong form of the energy (15) and the momentum equation (16) are multiplied by test functions $\delta\theta$ and η , respectively. After applying partial integration the weak form can be stated as:

$$\int_v \left[\rho \eta \cdot (\mathbf{a} - \hat{\mathbf{b}}) + \text{grad } \eta \cdot \sigma(\phi) \right] dv + \int_v \eta \gamma \kappa \frac{\text{grad } \tilde{c}}{[\tilde{c}]} dv + \int_v \delta\theta [\rho (c + L_\theta) \dot{\theta} - \rho r^s] dv + \int_v k \text{grad } \theta \text{ grad } \delta\theta dv = 0. \tag{29}$$

Surface tension has been accounted for with the Continuous Surface Force (CSF) model introduced by Brackbill et al. [5]. In the CSF model, the surface tension is transferred into a volume integral. The gradient of the color function \tilde{c} which is computed from the gradient of mass ensures that the volumetric surface force only acts in a small region close to the boundary or interface. The recoil pressure (21) could be incorporated in the same manner, but is neglected in the present analysis.

Following the standard Bubnov–Galerkin approach, the same shape functions are used to interpolate the primary variables as well as the test functions. The spatially discretized residual can then be written in the form:

$$\mathbf{M} \mathbf{a}_{n+1} + \mathbf{R}_u (\mathbf{u}_{n+1}) - \mathbf{P} + \mathbf{C} \dot{\theta}_{n+1} + \mathbf{R}_\theta (\theta_{n+1}) - \mathbf{Q} = 0 \tag{30}$$

In an Updated Lagrangian framework the support domain of the previous time step is considered the reference configuration of a material point at the current time step t_{n+1} . The shape functions are constructed in the reference configuration. The heat capacitance matrix \mathbf{C} is the same as in the explicit scheme, see (54). For a volumetric heat source, the power P_{pn+1} in the heat input vector \mathbf{Q} computes in analogy to (25) and (26). The coupling of OTM and ray tracing is discussed in Sect. 5.

The computation of the mass matrix \mathbf{M} , the internal forces \mathbf{R}_u and the thermal conductivity \mathbf{R}_θ follow standard procedures and can be found in the appendix in (55) and (56). For

the load vector \mathbf{P} it can be stated:

$$\mathbf{P} = \bigcup_{p=1}^{n_{mp}} \sum_{I=1}^{N_{pn}^{sup}} N_I(\mathbf{x}_{pn}) \left(m_p \hat{\mathbf{b}}_I - \mathbf{f}_n^{CSF} v_{pn+1} \right) \tag{31}$$

$$\mathbf{f}_n^{CSF} = \gamma \kappa_{pn} \frac{\mathbf{c}_{In}}{m_{In}}$$

The curvature κ_p is evaluated at each material point from the divergence of the nodal normals in the support domain. The nodal normal \mathbf{n}_I is computed by normalization of a color gradient \mathbf{c}_I which itself is defined as the nodal gradient of mass m_p :

$$\kappa_{pn} = \sum_{I=1}^{N_{pn}^{sup}} \text{div } \mathbf{n}_{In} \quad \mathbf{n}_{In} = \frac{\mathbf{c}_{In}}{\|\mathbf{c}_{In}\|} \tag{32}$$

$$\mathbf{c}_{In} = \sum_p \frac{N_I^{inf}(\mathbf{x}_{pn})}{\partial \mathbf{x}_{pn}} m_p$$

Brackbill et al. [5] and Chen et al. [6] point out that constructing the color gradient from a smoothed mass yields more accurate results. In the implementation of the CSF model into OTM, first the nodal color gradient is computed. Next, the nodal mass and the color gradient are smoothed independently of each other. Additionally the curvature κ_p is also smoothed. Smoothing is performed by averaging over the nodal or material point neighbors N_I^{nbr} or N_p^{nbr} , respectively. Five iterations were sufficient in our calculations. The algorithm is summarized in Fig. 6. Details are given in [30].

Weißenfels and Wriggers [29] have shown that the OTM suffers from insufficient integration. They have suggested a stabilization term for the momentum equation which is also employed in the current work. For this purpose the distance vectors $\mathbf{dx}_{Ipn+1}^{k+1}$ between nodes and material points are computed in each support domain. The distance vector in the current time step can also be obtained from the mapping of the distance vector \mathbf{dx}_{Ipn} of the previous time step with the incremental deformation gradient. If the solution of the momentum equation was correct, the difference between the two is zero. As a consequence of reduced integration this is not always fulfilled. The error is enforced to be zero by applying the penalty method:

$$\mathbf{E}_{In+1} = \varepsilon_s N_{Ipn} \frac{\mathbf{dx}_{Ipn+1} - \Delta \mathbf{F}_{pn+1} \mathbf{dx}_{Ipn}}{\|\mathbf{dx}_{Ipn}\|} \tag{33}$$

with $\mathbf{dx}_{Ipn} = \mathbf{x}_{In} - \mathbf{x}_{pn}$

The above defined tensor \mathbf{E} acts as an additional force and is added to the discretized weak form of the equation of motion (30). The influence of the penalty parameter ε_s on the accuracy of the solution has been studied extensively by

Fig. 6 Surface tension computation with OTM

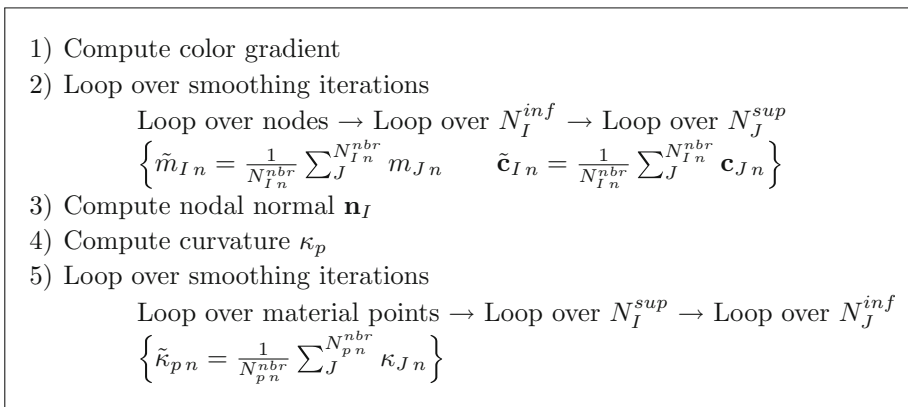
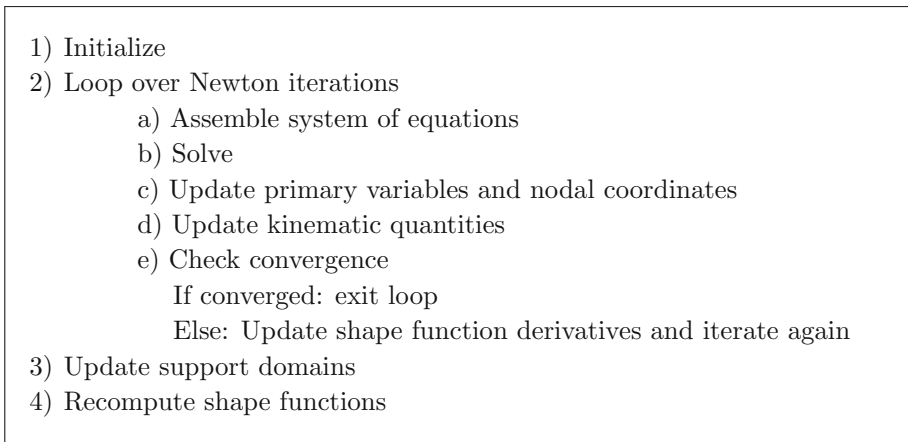


Fig. 7 Algorithmic implementation of a time step in OTM



Weißenfels and Wriggers [29] in various numerical examples.

In the implicit formulation the weak form (30) is evaluated at the next time step t_{n+1} . Acceleration and velocity are integrated with an implicit Newmark and the temperature derivative with a backward Euler time integration scheme with the constants $\gamma = 0.5$ and $\beta = 0.25$. Details on the Newmark time integration and the admissible range for γ and β can be found in standard FEM textbooks, e.g. [19]. The resulting non-linear equations are solved iteratively with a Newton–Raphson algorithm. The overall implicit stabilized OTM algorithm is sketched in Fig. 7.

4.3 Spatial discretization in OTM

The support domain of each material point is updated in every time step via a search algorithm. In this work, the search algorithm presented in [29] is employed. In every time step, the nodes which lie in a certain radius r_p around a material point p are identified by checking the condition:

$$S_{p n+1} = \left\{ \mathbf{x}_{I n+1} \mid \|\mathbf{x}_{I n+1} - \mathbf{x}_{p n+1}\| \leq \alpha r_p \right\}. \tag{34}$$

The search radius extension factor α controls the number of nodes inside the support domain. A particle distribution is regarded as admissible if all particles in each support domain $S := \bigcup_{p=1}^{n_{mp}} S_{p n+1}$ represent the whole body B_t without any spaces in between $B_t \subseteq S$. This requirement is met if the volume of a support domain v_p^{sup} is larger than the corresponding material point volume v_p . In 3D computations at least four nodes are necessary to form a convex hull around a material point. Additionally, in order to reduce the computational effort the size of support domains should be kept as low as possible. Further details can be found in [29].

In a Galerkin method shape or basis functions are necessary to interpolate the nodal data. For OTM, Li et al. [23] have suggested Local Maximum Entropy (LME) shape functions introduced by Arroyo and Ortiz [3]. They belong to the class of radial basis functions with an exponential ansatz:

$$Z_I(\mathbf{x}_p, \boldsymbol{\lambda}_p) = e^{-\beta_p \|\mathbf{x}_I - \mathbf{x}_p\|^2 + \boldsymbol{\lambda}_p(\mathbf{x}_p - \mathbf{x}_I)} \quad \beta_p = \frac{\gamma}{h_p^2} \tag{35}$$

The parameter β_p determines the locality of the LME shape functions and ensures a smooth transition from meshfree approximants to Delaunay affine basis functions, see e.g. [3]. Rosolen et al. [27] have indicated $\beta_p = [0.8/h_p^2, 4/h_p^2]$ as an optimal interval for the locality parameter. The character-

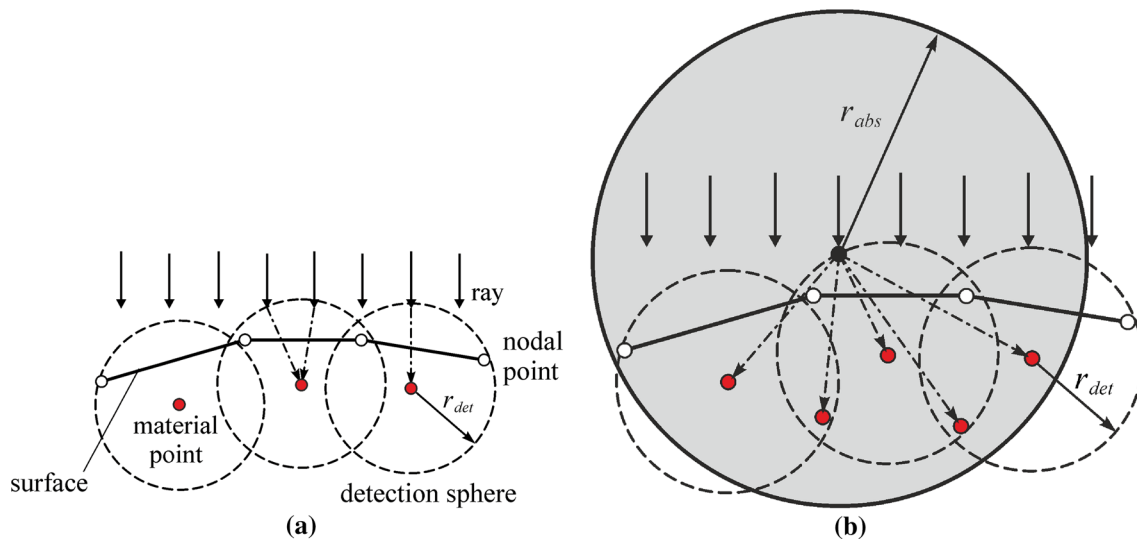


Fig. 8 Absorption of rays. **a** Direct absorption of at the material point that first detects a ray. **b** Redistribution of ray energy into a sphere with absorption radius r_{abs}

istic spacing h_p can be defined as twice the radius of a support domain, see [29]. The partition of unity is achieved by normalization, i.e. division by the sum Z of all nodal functions Z_J inside the support domain:

$$N_I = \frac{Z_I(\mathbf{x}_p, \lambda_p)}{Z}, \quad Z = \sum_{J=1}^{N_p^{sup}} Z_J(\mathbf{x}_p, \lambda_p) \quad (36)$$

The Lagrange multiplier λ_p has been introduced to meet the first order consistency criterion. It is computed from the constraint:

$$\mathbf{r}(\mathbf{x}_p, \lambda_p) = \sum_{I=1}^{N_p^{sup}} N_I(\mathbf{x}_p, \lambda_p) [\mathbf{x}_p - \mathbf{x}_I] = 0 \quad (37)$$

Note that the LME shape functions possess a weak Kronecker delta property. This means that it is only fulfilled on convex boundaries. For a mathematical explanation see [3] and for a graphical illustration in 2D [29].

5 Coupling of ray tracing and OTM

The laser strikes the surface of the irradiated part. This is why the irradiation is often expressed by a surface integral. To compute the required surface increments a triangulation of the free surface is necessary—a computationally very expensive operation. An additional challenge in meshfree methods is that surface nodes are not explicitly specified. In surface tension computations, this problem has been avoided by employing the Continuous Surface Force (CSF) model. This approach transforms the surface into a volume integral

which is only defined in the proximity of the free surface. Following the same motivation, the ray energy can be absorbed at material points near the free surface. This is implemented by defining a detection sphere at each material point, see Fig. 8a. Here, the detection radius r_p^{det} is set equal to the characteristic length of a support domain. The latter is obtained from the third root of material point volume v_p . A ray is absorbed by the material point that first detects it. The power P_p in the heat input vector \mathbf{Q} , see (25), is obtained from the summation of all incident rays at that material point:

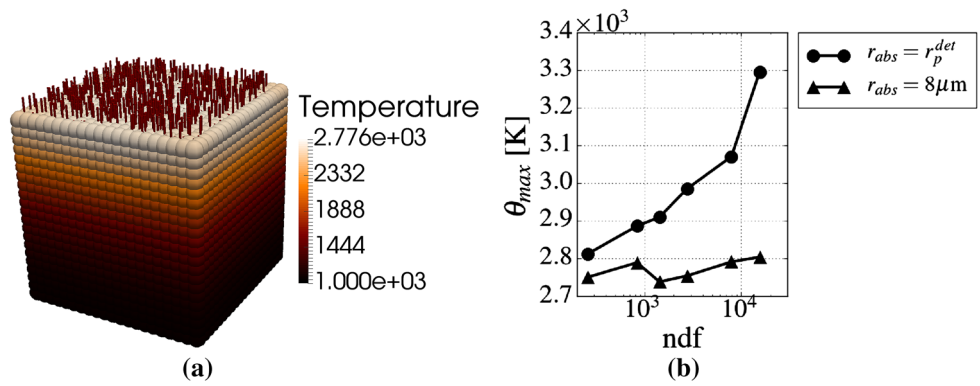
$$P_p = \rho_p r_p^s v_p = \sum_{r=1}^{n_{ray}} \begin{cases} (1 - R_r) \frac{E_r}{\Delta t} & \forall |\mathbf{x}_r - \mathbf{x}_p| < r_p^{det} \\ 0 & \text{else} \end{cases} \quad (38)$$

Here n_{ray} is the total number of rays. The ray energy E_r was defined in (6). The reflection coefficient R_r will be introduced later on in Sect. 5.3. For a graphical illustration of (38) see Fig. 8a.

As discussed in Sect. 2.1, the ray velocity \mathbf{v}_r is scaled by a factor k^{red} . It has to be chosen carefully in order to fulfill the Courant–Friedrichs–Lewy condition. In any given time step, a ray may not travel further than the average characteristic length of support domains. This measure can be obtained prior to the first time step from the cubic root of averaged material point volume \bar{v}_p . The admissible ray velocity is directly computed from the product of physical ray velocity and scaling factor k^{red} :

$$k^{red} |\mathbf{v}_r| \leq C \frac{\bar{v}_p^{1/3}}{\Delta t} \quad (39)$$

Fig. 9 **a** A cubic bloc with an edge length of $40 \mu\text{m}$ is irradiated with an uniform, rectangular heat source discretized into rays. **b** The maximum temperature in the block as a function of spatial OTM discretization with an absorption radius r_{abs} equal to and greater than r_p^{det}



The constant $C \in (0, 1]$ has been set to $2/3$. In the subsequent sections, the coupling of the ray tracing algorithm with the stabilized OTM method is discussed. Note that the presented coupling algorithm can easily be applied to other meshfree methods.

5.1 Influence of spatial OTM discretization

A perfectly insulated cubic block with an edge length of $40 \mu\text{m}$ is irradiated with a uniform, rectangular heat source. The laser beam is continuous. The setup is sketched in Fig. 9a. In order to satisfy the stability criterion from (28), the time increment in all simulations has been set to $\Delta t = 10^{-8}\text{s}$. The material data can be found in Table 2 and (51) and (52). The laser discretization has been chosen such that a further refinement does not affect the results ($\Delta t_r = 10^{-7}\text{s}$, $n_{rpl} = 500$).

The curve depicted in Fig. 9b shows that the maximum temperature increases with increasing number of nodal points. This can be explained mathematically by rearranging (38):

$$\rho_p r_p^s = \frac{1}{v_p} P_p = \frac{1}{h_p} \frac{P_p}{A_p} \sim \frac{1}{h_p} \tag{40}$$

In the above equation, the material point has been replaced by the product of characteristic length h_p and area A_p . Since the power P_p is proportional to A_p , the power per volume ($\rho_p r_p^s$) is inversely proportional to h_p .

For the coupled OTM ray tracing algorithm to converge, the power per volume needs to be independent of the OTM discretization. This can be achieved by distributing the incident ray energy within the neighborhood of a material point. The neighborhood can be modeled as a sphere with an absorption radius r_{abs} in the vicinity of a ray, see Fig. 8b. Inside the absorption sphere, the computation of the weights w_p^{abs} is based on a normalized Beer–Lambert law:

$$w_p^{abs} = \frac{Z_p}{\sum_q^{N_r^{abs}} Z_q} \tag{41}$$

$$Z_p = \begin{cases} e^{-\beta|\mathbf{x}_r - \mathbf{x}_p|/r_{abs}} & \forall |\mathbf{x}_r - \mathbf{x}_p| < r_{abs} \\ 0 & \text{else} \end{cases}$$

The use of a Beer–Lambert law can be motivated from the physical observation that the laser disperses into the irradiated body. In this work the optical extinction coefficient has been set to $\beta = 1$. The concept is graphically illustrated in Fig. 8b and the algorithmic implementation summarized in Fig. 12.

Figure 9b highlights that convergence of the maximum temperature is reached with the presented non-local distribution of ray energy. Within the considered range, the deviation of the maximum temperature decreases from 17.2% to only 2.4%. The influence of r_{abs} on maximum temperature is investigated in Sect. 5.4.

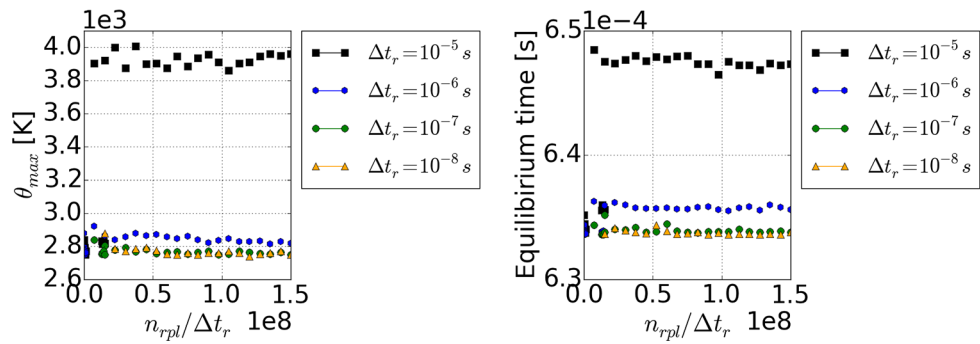
5.2 Laser discretization

The same perfectly insulated cubic block from the previous section is examined to study the influence of laser discretization in space and time. The block is discretized into 1422 nodes and 6587 material points. The laser beam is continuous in time and has a uniform, rectangular shape.

The ratio $n_{rpl}/\Delta t_r$ indicates the number of rays created per second. From a computational point of view, this ratio should be as small as possible in order to reduce cost. In Fig. 10, the maximum temperature and the time until equilibrium temperature is reached are plotted against the rays created per second. Four different time steps of ray creation Δt_r have been examined. The results suggest a time step size of ray creation Δt_r less or equal to ten times the simulation time step size Δt :

$$\frac{\Delta t_r}{\Delta t} \leq 10 \tag{42}$$

Fig. 10 Irradiation of a perfectly insulated cubic block, see Fig. 9a. Influence of laser discretization on maximum temperature (left) and on the time to achieve equilibrium temperature (right)



From Fig. 10 it can be deduced that 10^8 rays per second are enough to accurately discretize the laser beam, provided that the above condition is satisfied. To ensure convergence when an arbitrarily shaped part is irradiated, the laser spot must be accurately represented by absorption spheres with radius r_{abs} . The following criterion is proposed to estimate the necessary number of rays per level n_{rpl} to represent a laser spot of size A_{laser} :

$$n_{rpl} = \max \left(C \frac{A_{laser}}{\pi r_{abs}^2}, 50 \right) \quad (43)$$

Here C is a safety factor accounting for the random positioning of rays. Its value has to be always larger than 1 and is set to $C = 15$ in the current analysis. This is verified in Sect. 5.4.

5.3 Reflection

The computation of reflection exhibits two main challenges within meshfree methods: First, a surface needs to be defined in order to compute the direction of the emergent ray. Second, the position of incidence is unknown. In this work, it is traced back and set as anchor point \mathbf{x}_c of the surface. The surface normal \mathbf{n}_{refl} at the anchor point is then computed from the weighted material point normals in its vicinity. The advantage of this methodology is that reflection can be computed without the need of a surface triangulation, since the rays identify the free surface.

The anchor point \mathbf{x}_c is defined as the intersection of a ray trajectory with the detection sphere of a material point. It lays on the line segment of length Δs from the ray position of the previous time step $\mathbf{x}_r(t_{n-1})$ to the ray position of the current time step prior to reflection $\mathbf{x}_r(t_n^-)$. This is illustrated in Fig. 11a. The anchor point \mathbf{x}_c is approached iteratively:

$$\mathbf{x}_c^{j+1} = \mathbf{x}_c^j \begin{cases} + (\Delta s / 2^{j+1}) \cdot \mathbf{n}_r(t_n^-) & \forall |\mathbf{x}_c^j - \mathbf{x}_p| > r_p^{det} \\ - (\Delta s / 2^{j+1}) \cdot \mathbf{n}_r(t_n^-) & \forall |\mathbf{x}_c^j - \mathbf{x}_p| < r_p^{det} \end{cases} \quad (44)$$

In the first iteration, \mathbf{x}_c^0 is initialized with the ray position prior to reflection. Ten iterations of (44) are sufficient. In order to keep the computational effort as low as possible, the surface normal \mathbf{n}_{refl} at \mathbf{x}_c is approached by the normal vector at the current ray position $\mathbf{x}_r(t_n^-)$. It is obtained by weighting the N_p^{abs} material point normals \mathbf{n}_p inside the absorption radius r_{abs} . These are computed from the normalized gradient of mass. Unlike in the CSF implementation, the gradient of mass \mathbf{c}_p is now computed in the support domain:

$$\mathbf{n}_{refl} = \sum_p^{N_p^{abs}} \mathbf{n}_p w_p^{norm} \quad \mathbf{n}_p = \frac{\mathbf{c}_p}{|\mathbf{c}_p|} \quad \mathbf{c}_p = \sum_I^{N_p^{sup}} \frac{\partial N_I(\mathbf{x}_p) m_p}{\partial \mathbf{x}_p} \quad (45)$$

This approximation acts as a smoothing of material point normals with the weights w_p^{norm} :

$$w_p^{norm} = \frac{Z_p}{\sum_{q=1}^{N_p^{abs}} Z_q} \quad Z_p = \begin{cases} e^{-|\mathbf{x}_p - \mathbf{x}_r|/r_{abs}} & \forall |\mathbf{x}_p - \mathbf{x}_r| < r_{abs} \\ 0 & \text{else} \end{cases} \quad (46)$$

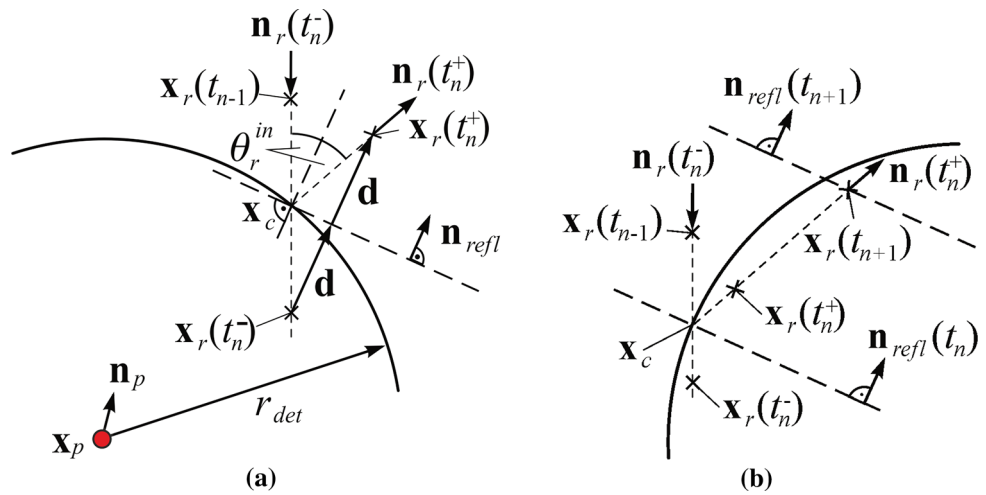
Based on the assumption that the emergent is equal to the incident angle, the ray positions are updated via:

$$\mathbf{x}_r(t_n^+) = \mathbf{x}_r(t_n^-) + 2\mathbf{d} \quad \mathbf{d} = [(\mathbf{x}_c - \mathbf{x}_r(t_n^-)) \cdot \mathbf{n}_{refl}] \mathbf{n}_{refl} \quad (47)$$

The vector \mathbf{d} is a projection of the vector pointing from the ray position prior to reflection to the anchor point \mathbf{x}_c onto the surface normal \mathbf{n}_{refl} , see Fig. 11a. The direction of the ray after reflection $\mathbf{n}_r(t_n^+)$ and the angle of incidence θ_r^{in} are obtained from:

$$\mathbf{n}_r(t_n^+) = \frac{\mathbf{x}_r(t_n^+) - \mathbf{x}_c}{|\mathbf{x}_r(t_n^+) - \mathbf{x}_c|} \quad \theta_r^{in} = \arccos \frac{\mathbf{n}_r(t_n^-) \cdot \mathbf{n}_{refl}}{|\mathbf{n}_r(t_n^-) \cdot \mathbf{n}_{refl}|} \quad (48)$$

Fig. 11 **a** A surface is constructed from the OTM discretization at the anchor point \mathbf{x}_c in order to compute the reflection. **b** The ray is reflected in time step t_n . It can not leave the detection sphere within one time step, i.e. the scalar product $(\mathbf{n}_r(t_n^+) \cdot \mathbf{n}_{refl}(t_{n+1}))$ is positive. Therefore, the ray proceeds without being reflected



```

1) Compute material point normals (equation 45)
2) If  $(\Delta t_r \% \Delta t == 0)$ : Initialize new layer of rays (equation 6)
3) Loop over rays  $r$ :
    Update ray positions (equation 8)
    Loop over material points  $q$ :
        If  $|\mathbf{x}_r - \mathbf{x}_q| < r_q^{det}$ :
            Compute anchor point  $\mathbf{x}_c$  (equation 44)
            Loop over material points  $p$ :
                If  $|\mathbf{x}_r - \mathbf{x}_p| < r_{abs}$ :
                    Assemble weights  $w_p^{abs}$  and surface normal  $\mathbf{n}_{refl}$  (equation 41 and 45)
                    Store index of absorbing material point in list
            Normalize weights  $w_p^{abs}$  and  $\mathbf{n}_{refl}$  (equation 41 and 45)
            If  $\text{sgn}(\mathbf{n}_r \cdot \mathbf{n}_{refl}) < 0$ :
                Compute reflectivity  $R_r$  (equation 48 and 49)
                Update the reflected ray's position, energy and direction (equation 47 and 48)
            Loop over absorbing material points  $p$ :
                Distribute ray power:  $P_{p+} = (1 - R_r) \frac{\Delta E_r}{\Delta t} w_p^{abs}$ 
    
```

Fig. 12 Algorithmic implementation of the coupled ray tracing OTM algorithm including ray absorption and reflection. The efficiency of the algorithm can be improved using linked lists or linked cells, see e.g. [12]

The energy associated with a reflected ray computes from the reflectivity R_r . It can be derived from the Fresnel-equations, see e.g. [38], and yields:

$$R_r = \frac{1}{2} \left[\left(\frac{\hat{n}^2}{\hat{\mu}} \cos \theta_r^{in} - (\hat{n}^2 - \sin^2 \theta_r^{in})^{1/2} \right)^2 + \left(\frac{\hat{n}^2}{\hat{\mu}} \cos \theta_r^{in} + (\hat{n}^2 - \sin^2 \theta_r^{in})^{1/2} \right)^2 \right] + \left(\frac{\cos \theta_r^{in} - \frac{1}{\hat{\mu}} (\hat{n}^2 - \sin^2 \theta_r^{in})^{1/2}}{\cos \theta_r^{in} + \frac{1}{\hat{\mu}} (\hat{n}^2 - \sin^2 \theta_r^{in})^{1/2}} \right)^2 \quad (49)$$

The ratios of magnetic permeabilities and refractive indices in the absorbing and the surrounding medium are denoted

$\hat{\mu}$ and \hat{n} , respectively. A graphical illustration of the function $R(\theta_r^{in}, \hat{n}, \hat{\mu} = 1)$ can be found in [38]. In this work, the reflectivity (49) has been implemented with the constant values $\hat{\mu} = 1$ and $\hat{n} = 2.4$.

Note that the speed of reflected rays may be too low to leave the detection sphere within one time step. To guarantee that a reflected ray is not reflected again before it has left the detection sphere, the sign of the scalar product $(\mathbf{n}_r \cdot \mathbf{n}_{refl})$ is checked. A positive sign indicates an already reflected and a negative sign an incident ray. This is illustrated in Fig. 11b. The algorithmic implementation of the ray tracing scheme is summarized in Fig. 12.

Table 1 Results of sphere irradiation test case

	Beer–Lambert	Corr. Beer–Lambert	Ray tracing
Absorbed energy	0.152 mJ	0.206 mJ	0.206 mJ
Maximum temperature	1520 K	1758 K	2528 K
Equilibrium time	0.205 ms	0.207 ms	0.249 ms

5.4 Comparison of heat source modeling

A sphere with a radius of 20 μm is irradiated for the duration $t_{irr} = 0.1$ ms. The sphere is discretized into 343 nodes and 1465 material points. The time step size in all simulations is $\Delta t = 10^{-7}$ s. The radial intensity distribution of the laser energy follows a normalized Gaussian distribution (see Eq. 5). The beam radius is $R = 20$ μm and the laser power of the constant beam is given by $P_{laser} = 2.5$ W. The resulting temperature evolution using a Beer–Lambert type heat source and the ray tracing scheme are compared. With the ray tracing scheme, the absorption radius is $r_{abs} = 8$ μm and reflection is computed as described in Sect. 5.3.

It has been found that 82% of the emitted energy were absorbed with the ray tracing scheme. This result has been validated by comparison with the theoretical value of 81.3% obtained with the software Mathematica, see (58) and (59) in the appendix for details. Hence, in the Beer–Lambert model a static absorption coefficient $\zeta = 0.82$ has been used. The powder bed depth L in (13) is equal to the diameter of the sphere, i.e. $L = 40$ μm .

As was graphically illustrated in Fig. 3b, the geometry of the sphere and the volumetric intensity distribution do not fully overlap. To overcome this issue, the following correction is introduced:

$$I^{corr}(r, z) = I(r, z) \frac{\pi R^2 L}{v_h^{HAZ}} \quad (50)$$

Here $\pi R^2 L$ is the cylindrical volume affected by the intensity function $I(r, z)$ with R the laser beam radius. The discretized volume of the actual heat affected zone is denoted v_h^{HAZ} . The influence of the corrected intensity distribution (50) is evaluated in Table 1 and graphically illustrated in Fig. 13a and b. Without correction, about 25% less energy is absorbed by the sphere. However, the difference in equilibrium time is negligible. The reason is that the laser power is quite evenly distributed inside the volume according to the Beer–Lambert law. With the volumetric heat source, increasing the power does not cause significantly larger temperature gradients.

The results obtained with the ray tracing scheme are depicted in Fig. 13c and d. In Fig. 13c a very fine laser discretization has been used with $\Delta t_r = \Delta t$ and $n_{rpl} = 250$. In Fig. 13d the laser discretization has been chosen according to Eqs. 42 and 43 yielding to $\Delta t_r = 10\Delta t$ and $n_{rpl} = 94$. The convergence study in Fig. 14 shows that the criteria used to

estimate the optimal laser discretization are valid. The maximum temperature obtained with $\Delta t_r = 10\Delta t$ only deviates about 2.42% compared to the smaller time step $\Delta t_r = \Delta t$ if n_{rpl} is chosen appropriately. Comparing the ray tracing approach with the volumetric heat source, it can be seen that the heat input is much more localized. The maximum temperature is about 66% higher and it takes 20% longer to achieve equilibrium time, see Table 1. Even the maximum temperature and the consolidation time obtained with the corrected volumetric heat source heavily differ from the ray tracing results.

Additionally, in Fig. 15a the influence of the absorption radius r_{abs} is illustrated. For small values of r_{abs} , the heat input is strongly localized yielding to an increase of maximum temperature. When larger values of r_{abs} are used, the laser is allowed to disperse deeper into the part. The heat is distributed more evenly and, as a consequence, the maximum temperature is lower. With a further increase of r_{abs} , θ_{max} converges towards a horizontal asymptote. In the outline of this work, the absorption radius has been set to $r_{abs} = 8$ μm .

Note that in this simple numerical example the CPU time using ray tracing is with 128% increase dramatically higher as compared to the volumetric heat source approach. This is due to the simplicity of the spherical geometry and its coarse spatial discretization. When the thermo-mechanical problem is solved and the number of degrees of freedom increases as in the example discussed in Sect. 6, the additional computational effort is only about 3.3%.

5.5 Investigation of laser pulsing

The effect of laser pulsing on maximum temperature has been studied for the insulated sphere in the previous section. A rectangular laser pulse is assumed, see (2). Irradiation time and laser power have been set to $t_{irr} = 0.1$ ms and $P_{laser} = 0.25$ W, respectively. In Fig. 15b, the maximum temperature is plotted as a function of the pulsing width Δt_{puls} . The effect of varying repetition rates $f_{rep} = \{50, 100, 200\}$ kHz is also investigated.

As graphically illustrated in Fig. 2, at a constant repetition rate a smaller pulsing period yields a higher pulsing power. Per consequence, the maximum temperature decreases exponentially with increasing pulsing period. At a fixed pulsing period, the pulsing power decreases with increasing repe-

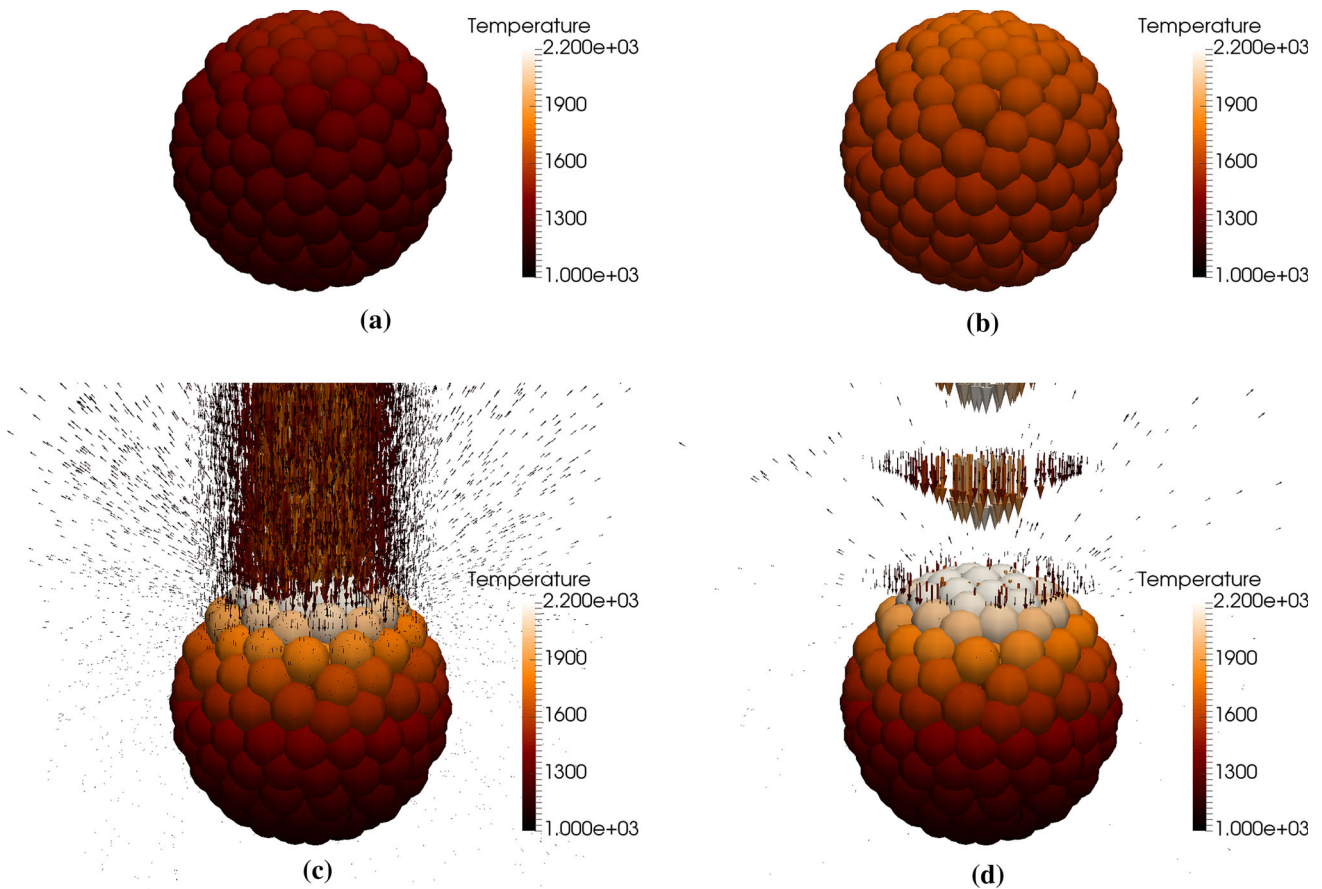
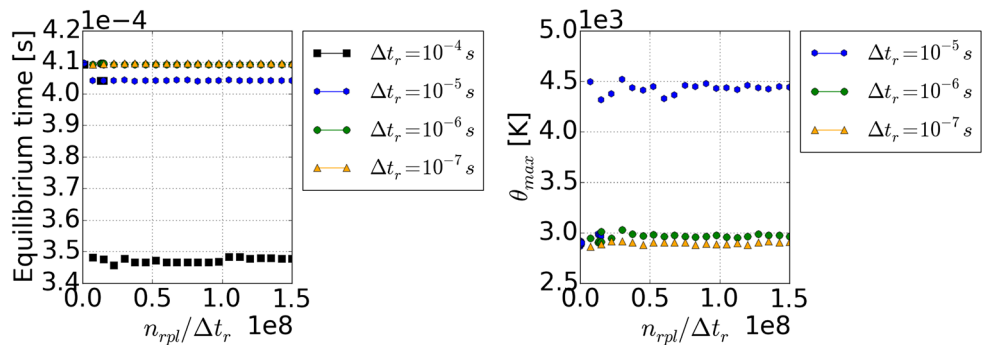


Fig. 13 Temperature distribution at $T = 0.1$ ms caused by laser irradiation with $P_{laser} = 2.5$ W. **a** Beer-Lambert. **b** Corrected Beer Lambert. **c** High resolution ray tracing. **d** Sufficient ray discretization

Fig. 14 Influence of the ray discretization on the time to achieve equilibrium temperature (left) and on the maximum temperature (right). The time increment of the thermal problem is $\Delta t = 10^{-7}$ s



tion rate and the resulting maximum temperature drops. These effects are displayed by the curves in Fig. 15b.

Zohdi [41] has shown that in addition to a pulsing heat source a thermally relaxed heat equation is necessary to accurately predict heat waves. However, this requires the relaxation time as an additional model parameter. While Mumtaz and Hopkinson [26] have investigated the effect of pulsing laser beams on the surface quality of SLM fabricated parts experimentally, in practice often continuous laser beams are used. The particle fusion analysis presented in Sect. 6 is restricted to this case.

6 Laser irradiation and melting of metal powder particles

The importance of heat source modeling in SLM process simulation is illustrated by means of a simple numerical test case. It consists of two metal powder particles laying on a solid substrate. The thermal and mechanical contact is modeled with a penalty regularization as discussed in the appendix. As sketched in Fig. 16, a continuous laser travels from 20 μm in front of the part to 20 μm behind it. The beam radius is $R = 60 \mu\text{m}$ and the scan speed $v_{laser} = 0.2 \text{ ms}^{-1}$. Hence,

Fig. 15 **a** Influence of absorption radius r_{abs} on maximum temperature. **b** The effect of laser pulsing on maximum temperature (dotted) compared to a continuous laser beam (solid line) with $\Delta t = \Delta t_r = 10^{-8}$ s and $t_{irr} = 0.1$ ms

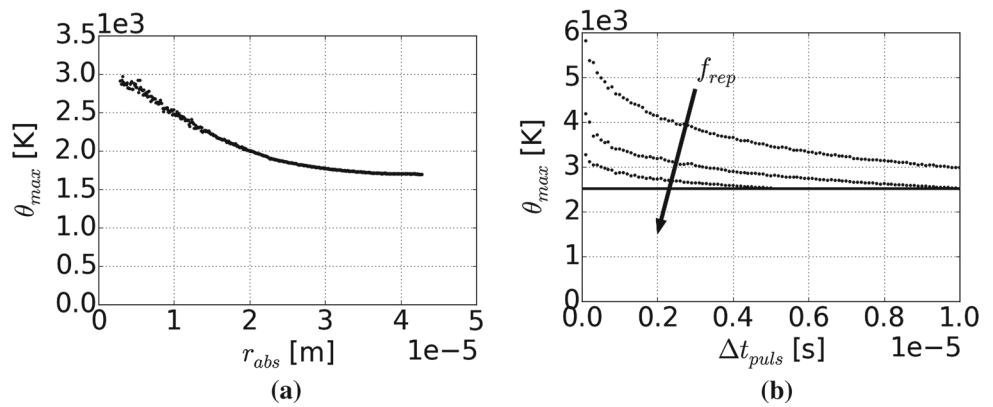


Table 2 Material properties, laser specifications and numerical parameter

	Symbol	Value
<i>Thermomechanical parameter</i>		
Poisson's ratio	ν	0.25
Compression modulus	K	0.13 GPa
Viscosity of molten metal	η	0.1 kg/(s m)
Surface tension coefficient	γ	1.7 N/m
Thermal expansion coefficient	α_{th}	1.75×10^{-3}
Latent heat of melting (vaporization)	L_m (L_v)	0.299 MJ/kg (6.09 MJ/kg)
Melting (evaporating) temperature	T_{melt} (T_{vap})	1770 K (3130 K)
Initial density	ρ_0 ($\theta_{ini} = 300$ K)	7900 kg/m ³
<i>Laser parameter</i>		
Scan rate	v_{laser}	0.2 m/s
Laser beam radius	R	60 μ m
<i>Gusarov parameter</i>		
Optical thickness	λ	2
Hemispherical reflectivity	ρ_h	0.7
Powder bed depth	L	40 μ m
Particle diameter	D	40 μ m
<i>Numerical parameter</i>		
Stabilization parameter	ε_s	10^{-8}
Contact parameter	ε_c	3×10^6
LME constant	γ	1.2

the irradiation time is $t_{irr} = 600 \mu$ s. A time step size of $\Delta t = 1 \mu$ s is used for the implicit thermo-mechanical simulations, i.e. the laser irradiation is discretized into 600 time steps. Due to the relatively large time step size Δt , a further reduction of the time step size of ray creation Δt_r is not appropriate. When smaller time step sizes are used, reducing Δt_r according to (42) is a promising option to limit the computational time. The beam is discretized according to (43) with $A_{laser} = 3.2 \times 10^{-9}$ m² into $n_{rpl} = 238$ rays per level and the geometry into 1691 nodes and 7441 material points. Convergence of the stabilized OTM method for the aforementioned spatial and temporal discretization has been shown in [30]. The thermal conductivity

$$k = \begin{cases} (0.0135 \frac{1}{K} \cdot \theta + 9.345) \frac{W}{mK} & \forall \theta \in [300, T_m] \\ 32.4 \frac{W}{mK} & \forall \theta > T_m \end{cases} \quad (51)$$

and the heat capacity

$$c = \begin{cases} (0.258 \frac{1}{K} \cdot \theta + 376.406) \frac{J}{kg} & \forall \theta \in [300, T_m] \\ 815 \frac{J}{kg} & \forall \theta > T_m \end{cases} \quad (52)$$

are simplifications of the data reported by The International Nickel Company [28]. The remaining material and process data are summarized in Table 2. Further details on the material parameters used in the simulations can be found in [30].

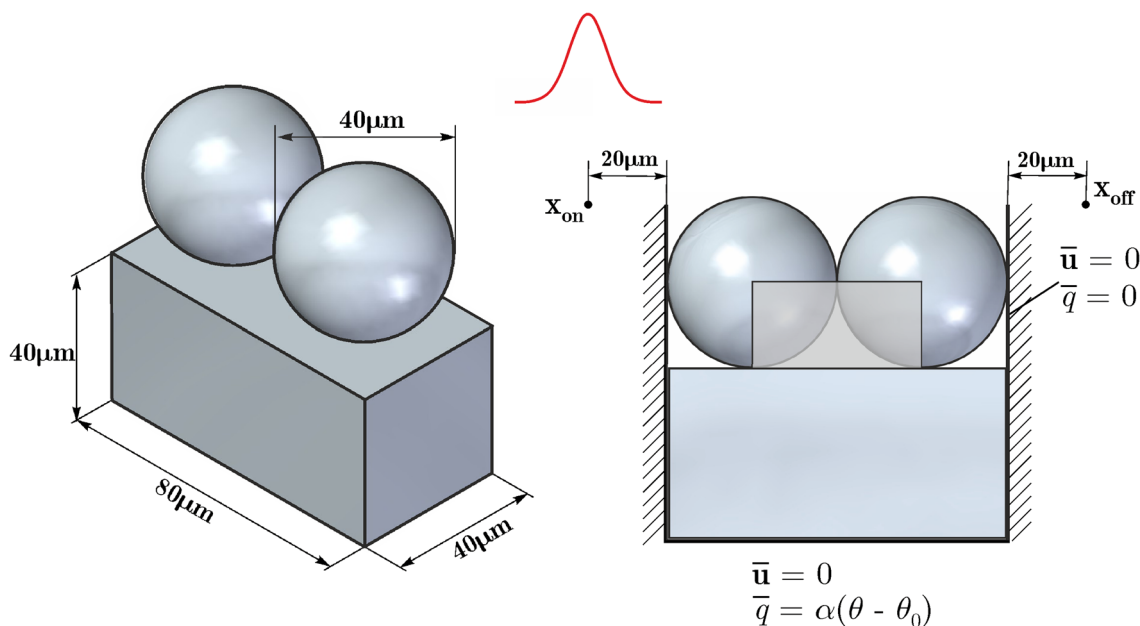


Fig. 16 Left: metal particle fusion test case. Laser irradiation starts at the position x_{on} and ends at x_{off} . Right: definition of the gap indicator as one minus the metal volume divided by the volume of the transparent box

The results obtained with the ray tracing algorithm and the Gusarov-type volumetric heat source are compared by means of a parameter study. For this purpose, multiple parameter sets have been simulated in parallel.

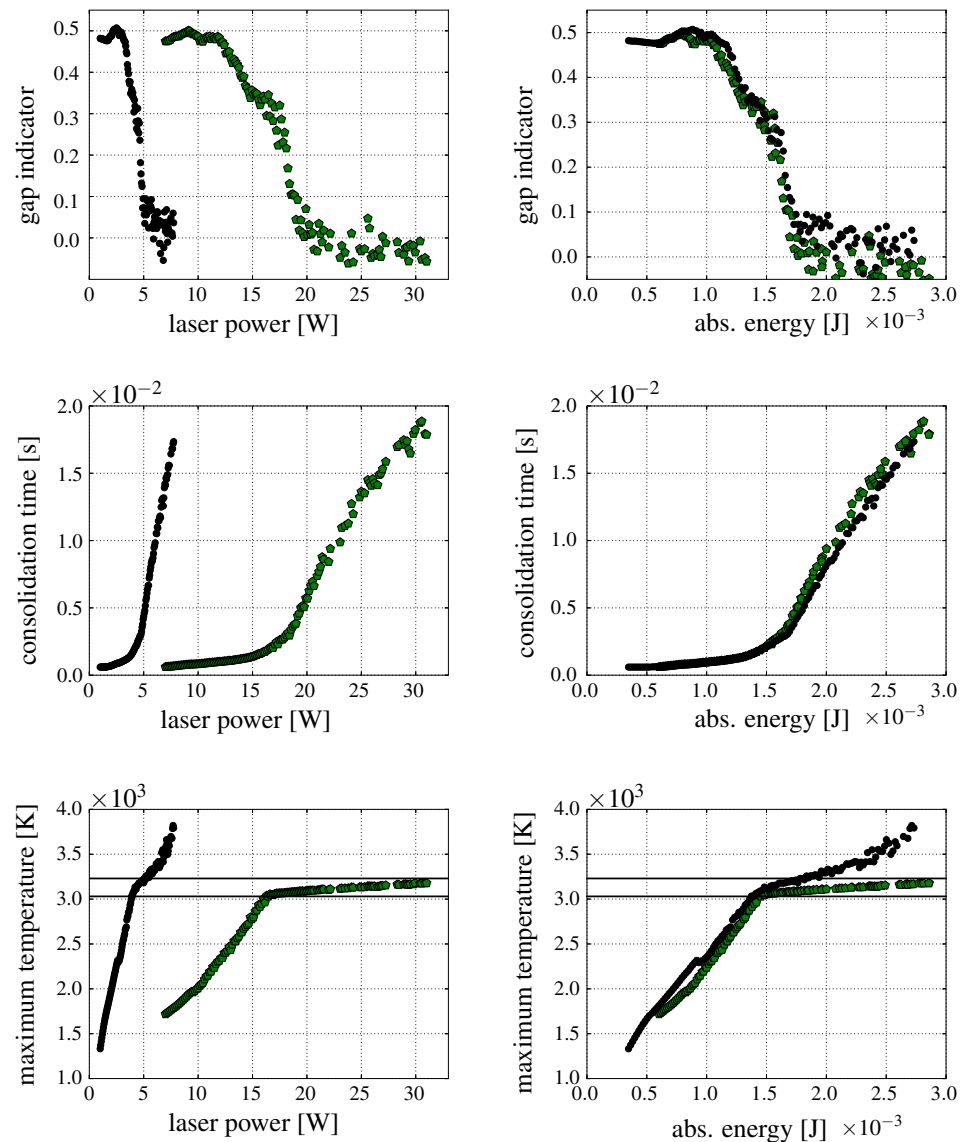
The fusion of metal powder particles is investigated by means of a gap indicator, the maximum temperature occurring during laser irradiation and the consolidation time. The latter is measured as the time until all nodal temperatures have dropped below the melting point. The gap indicator provides a measure of the fusion bond and is graphically illustrated in Fig. 16. It is defined as one minus the ratio of metal volume that lays inside a box spanned by the two midpoints of the powder particles and the initial surface of the solid substrate. In the initial state, the gap indicator Π is equal to one minus the packing density:

$$\Pi = 1 - \frac{v_{metal}}{v_{box}} \approx 0.48 \tag{53}$$

The three quantities of interest are plotted as a function of laser power and absorbed energy in Fig. 17. When plotted against the laser power, the difference between ray tracing and volumetric Gusarov model is significant. Two reasons are responsible for this difference: First, in the Gusarov model, a bell-like radial intensity distribution has been used, see (10), while a Gaussian distribution was assumed with the ray tracing model, see (5). Second, and most importantly, at the same laser power less energy is distributed into the part with the Gusarov model. This is due to the insufficient overlap of volumetric intensity distribution and geometry.

Figure 18 shows that the absorbed energy linearly depends on the laser power. Note that the absorbed energy is an outcome of the simulation and depends on the heat source formulation. Only the laser power can be used as an input parameter. When plotted against the absorbed energy, gap function and consolidation time are nearly identical for both heat source models. An important difference exists in the maximum temperature evolution. With both schemes, the maximum temperature increases up to a kink, where the slope of the curve drastically decreases. This is the onset of vaporization. The absorption of latent heat in the temperature interval around the boiling point $T_v = 3130$ K delays the maximum temperature evolution. With the ray tracing scheme, the slope within this region is larger compared to the Gusarov-type heat source. After leaving the absorption interval, the slope of the maximum temperature increases. The difference in the evolution of the maximum temperature can be explained graphically from Fig. 19. With both heat source models, the same amount of energy has been absorbed by the system. Using the volumetric heat source, the heat is more evenly distributed. Vaporization occurs homogeneously within a relatively large region. The maximum temperature lies within the absorption interval of latent heat of vaporization. Using ray tracing, the heat input is much more localized, leading to a small region near the surface where the metal is vaporized. In the simulations, vaporized material points have not been removed from the computations but modeled as melt, so that the final geometry looks identical to the one obtained with the volumetric heat source.

Fig. 17 Gap function, cooling time and maximum temperature as a function of laser power (left) and absorbed energy (right) with $\alpha_{\text{powder}} = 10^3 \text{ W}/(\text{m}^2 \text{ K})$. The results obtained with the ray tracing algorithm (black dots) are compared to those when a Gusarov-type heat source (green pentagon) is used. The solid lines in the third row mark the interval in which the latent heat of vaporization is absorbed. (Color figure online)



Nevertheless, the dramatic effect of heat source modeling on vaporization is illustrated.

The simulations highlight two key advantages of ray tracing over volumetric heat source approaches: First, the absorbed energy can be computed much more precisely based on the Fresnel equations. Second, a local layer of vaporization can be predicted. Numerical parameters in the Fresnel equations and the absorption radius can be adjusted to fit experimentally measured results independently of the irradiated geometry.

7 Conclusion

A coupling scheme for ray tracing and meshfree methods has been established. In order to avoid a computationally expen-

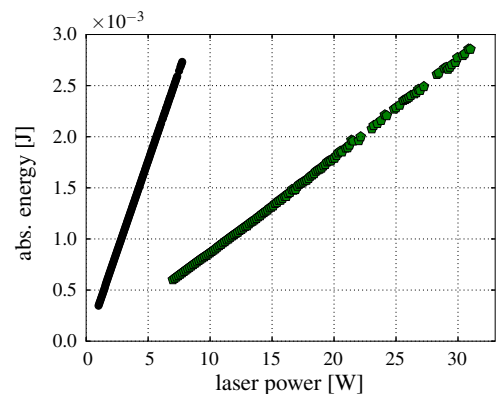


Fig. 18 Absorbed energy as a function of laser power with the ray tracing scheme (black dots) and a volumetric heat source (green pentagons). (Color figure online)

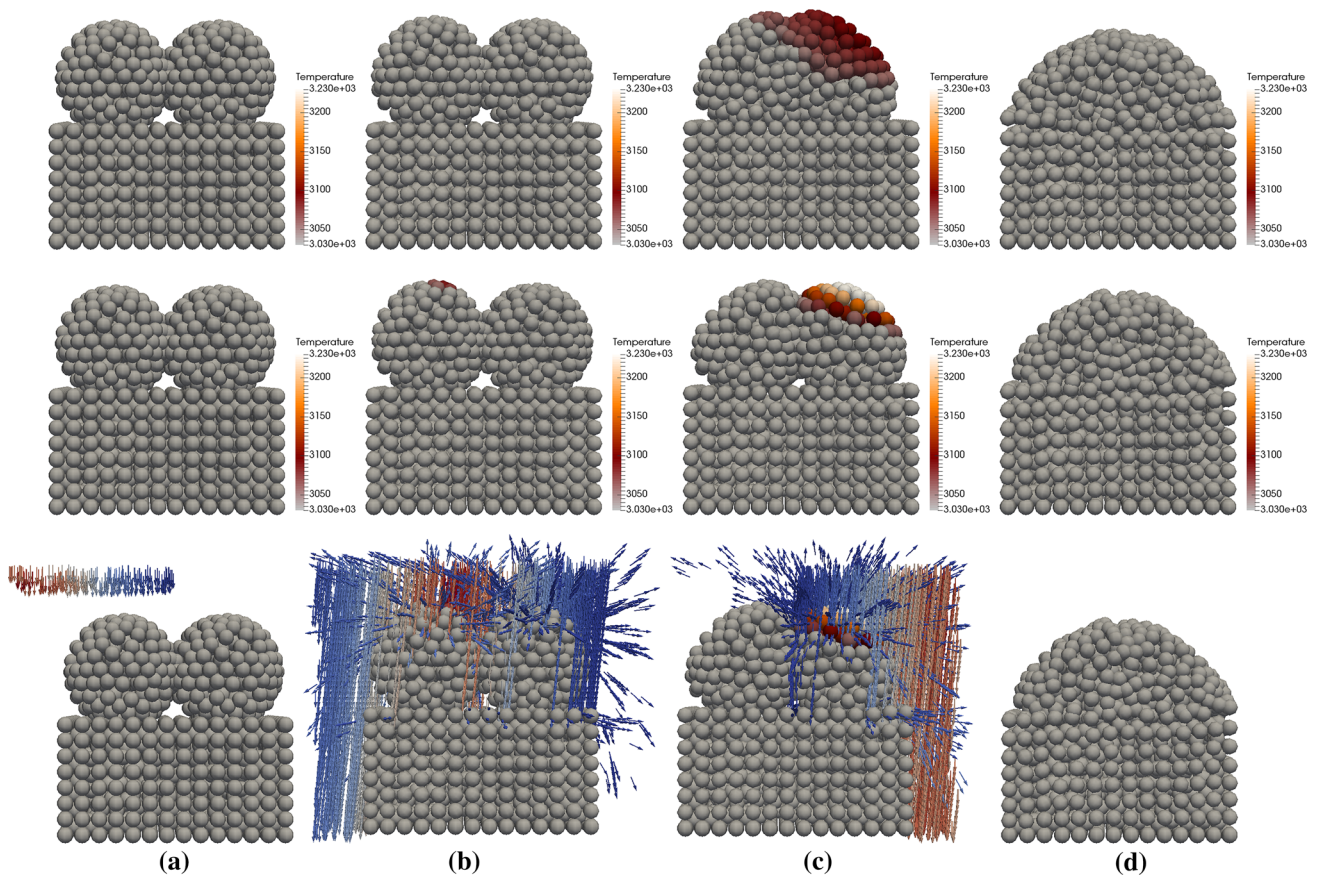


Fig. 19 Melting and solidification of two laser irradiated metal particles that absorb the energy 1.97 mJ. On the top, the laser is described with a volumetric heat source and in the middle and on the bottom with the ray tracing algorithm. In the middle, the rays are hidden to highlight the

localized heat input. The temperature is scaled to the interval in which the latent heat of vaporization is absorbed. **a** $t = 0$ ms. **b** $t = 0.25$ ms. **c** $t = 0.6$ ms. **d** $t = 6.65$ ms

sive surface triangulation, the rays are used to identify the free surface. To ensure convergence, a non-local formulation for the absorption of rays is presented. A parameter is introduced to control the locality of ray absorption. This parameter has a physical interpretation: It represents the penetration of laser radiation into the part. In order to determine the reflection, surface normals are computed from the gradient of mass. The approach is motivated from the well known Continuous Surface Force (CSF) model which is commonly applied to problems involving surface tension effects. While the presented method is easy to adopt for a variety of meshfree methods, the algorithm has exemplarily been implemented into the stabilized Optimal Transportation Meshfree (OTM) framework.

The ray tracing algorithm has been applied to a particle fusion analysis. Wessels et al. [30] have presented a numerical test case consisting of two metal powder particles placed on a solid substrate. By choosing appropriate boundary conditions, preliminary information about the processability window of SLM can be gained. The results with

the ray tracing algorithm were compared to those obtained with a volumetric heat source. It is illustrated that the overlap of volumetric intensity distributions and the curved geometry of a powder bed is insufficient and cannot be corrected. Furthermore, using ray tracing, the heat input is confined in the proximity of the irradiated surface while volumetric heat sources smear the absorbed energy within the part. This yields to an underestimation of vaporization. For the aforementioned reasons, ray tracing is the method of choice to simulate laser–matter interaction in SLM processes. The efficiency of the suggested algorithm enhances the applicability of ray tracing for meshfree methods.

Acknowledgements This work was supported by the compute cluster, which is funded by the Leibniz Universität Hannover, the Lower Saxony Ministry of Science and Culture (MWK) and the German Research Association (DFG). Henning Wessels acknowledges the generous support of the Fulbright association for an internship in the group of Prof. Tarek I. Zohdi at the University of California, Berkeley.

Appendix

Discrete matrices

With the Kronecker delta δ_{IJ} , the heat capacity and the conductivity matrices \mathbf{C} and \mathbf{K} are defined by:

$$\mathbf{C} = \bigcup_{p=1}^{n_{mp}} \sum_{I=1}^{N_{pn}^{sup}} \sum_{J=1}^{N_{pn}^{sup}} N_I(\mathbf{x}_{pn}) \delta_{IJ} m_p c_{pn} \quad (54)$$

$$\mathbf{K} = \bigcup_{p=1}^{n_{mp}} \sum_{I=1}^{N_{pn}^{sup}} \sum_{J=1}^{N_{pn}^{sup}} \frac{N_I(\mathbf{x}_{pn})}{\partial \mathbf{x}_{pn}} \frac{N_J(\mathbf{x}_{pn})}{\partial \mathbf{x}_{pn}} k_{pn} v_{pn}$$

Note that a lumped heat capacity matrix has been used in order to reduce the under- and overshoots produced numerically in the presence of sharp temperature gradients as suggested in [7]. Details on the lumping concept can be found in [19].

In the implicit scheme, the lumped mass matrix \mathbf{M} computes from:

$$\mathbf{M} = \bigcup_{p=1}^{n_{mp}} \sum_{I=1}^{N_{pn}^{sup}} \sum_{J=1}^{N_{pn}^{sup}} N_I(\mathbf{x}_{pn}) \delta_{IJ} m_p \quad (55)$$

The internal forces \mathbf{R}_u and the thermal conduction \mathbf{R}_θ are formulated as a function of the unknown current values of the primary variables:

$$\mathbf{R}_u = \bigcup_{p=1}^{n_{mp}} \sum_{I=1}^{N_{pn}^{sup}} \sum_{J=1}^{N_{pn}^{sup}} \mathbf{B}_{IJ}^T \sigma_{IJn+1}$$

$$\mathbf{R}_\theta = \bigcup_{p=1}^{n_{mp}} \sum_{I=1}^{N_{pn}^{sup}} \sum_{J=1}^{N_{pn}^{sup}} \frac{N_I(\mathbf{x}_{pn})}{\partial \mathbf{x}_{pn+1}} \frac{N_J(\mathbf{x}_{pn})}{\partial \mathbf{x}_{pn+1}} k_{pn} v_{pn+1} \theta_{Jn+1} \quad (56)$$

The definition of the \mathbf{B} -matrix can be found for instance in [31]. Although the shape functions of the previous time step are used, their derivatives are computed with respect to the current material point coordinate \mathbf{x}_{pn+1} :

$$\frac{\partial N_I(\mathbf{x}_{pn+1})}{\partial \mathbf{x}_{pn+1}} \approx \frac{\partial N_I(\mathbf{x}_{pn})}{\partial \mathbf{x}_{pn}} \frac{\partial \mathbf{x}_{pn}}{\partial \mathbf{x}_{pn+1}} \quad (57)$$

$$= \frac{\partial N_I(\mathbf{x}_{pn})}{\partial \mathbf{x}_{pn}} (\Delta \mathbf{F}_{pn+1})^{-1}$$

In the above equation, the incremental deformation gradient $\Delta \mathbf{F}$ has been defined. Since a reference configuration is not stored, $\Delta \mathbf{F}$ is used to update the deformation gradient.

The computation of the stress tensor follows the constitutive equations defined in Sect. 3. Details on the update of kinematic quantities can be found in [30].

Absorption validation

The power fraction ζ absorbed by a hemisphere is computed from the surface integral:

$$\zeta = \int_0^R \int_0^{2\pi r} (1 - R_r(\theta^{in})) I_{rad}(r) d\phi dr \quad (58)$$

With the radial intensity function from (5) and the substitutions $r = R \sin(\theta^{in})$ and $dr = R \cos(\theta^{in})$ one obtains:

$$\zeta = \int_0^{\frac{\pi}{2}} (1 - R_r(\theta^{in})) 4 \frac{\sin(\theta^{in}) \cos(\theta^{in})}{1 - e^{-2}} d^{in} \quad (59)$$

The definite integral has been evaluated with the software Mathematica using $R_r(\theta^{in})$ from (49) with the parameters $\hat{\mu} = 1.0$ and $\hat{n} = 2.4$. The result ($\zeta = 81.3\%$) is in very good agreement with the coupled ray tracing OTM algorithm ($\zeta = 82\%$) from Sect. 5.4.

Contact formulation

In the momentum equation, frictionless contact with a rigid wall is modeled using a penalty regularization. The contact force acting at a node is approximated by the normal penetration g_I and the penalty parameter ε_c :

$$\mathbf{R}_{In+1}^{con} = \varepsilon_c g_{In+1} \cdot \mathbf{n}_I \quad g_{In+1} = (\mathbf{x}_{In+1} - \bar{\mathbf{x}}_I) \cdot \mathbf{n}_I \quad (60)$$

The gap g_{In+1}^{k+1} is defined as the distance between the nodal solution and the prescribed boundary displacement $\bar{\mathbf{x}}_I$. The normal \mathbf{n}_I and the prescribed boundary displacement $\bar{\mathbf{x}}_I$ are constant in time.

In the energy equation, a linear temperature profile is assumed from the boundary temperature θ to a region in distance h where the temperature is in equilibrium, i.e. $\theta_0 = const.:$

$$\bar{q} = -k \text{grad } \theta \approx -k \frac{(\theta - \theta_0)}{h} \quad (61)$$

This formulation is analogous to Newton's law of cooling that is commonly employed to model convective boundary conditions. It is referred to as Robin boundary condition and can be added to the strong form of the energy equation as a surface flux. The quotient k/h is the heat transfer coefficient α . Its influence on the results of a metal particle fusion simulation has been studied in detail in [30]. Since rigid contact is assumed, the contact area is constant throughout the

simulation. In OTM, the initial configuration is a tetrahedral mesh. Hence, a triangulation of the initial surface is already known. The increment dA_I related to an integration point \mathbf{x}_I on the triangulated surface follows from the norm of the cross product of nodal coordinates \mathbf{x}_I . Nodal surface increments can be interpolated from:

$$dA_I = \sum_{l=1}^3 \frac{1}{3} dA_l \quad dA_I = \frac{1}{2} |(\mathbf{x}_1 - \mathbf{x}_2) \times (\mathbf{x}_3 - \mathbf{x}_2)| \quad (62)$$

This yields to a node-wise imposition of the Robin boundary condition:

$$\mathbf{R}_{In+1}^{\theta k+1} = -\alpha \left(\theta_{In+1}^{k+1} - \theta_0 \right) dA_I \quad (63)$$

A deeper insight into computational contact mechanics can be found in [32].

References

1. Ammer R, Markl M, Ljungblad U, Körner C, Råde U (2014) Simulating fast electron beam melting with a parallel thermal free surface lattice Boltzmann method. *Comput Math Appl* 67(2):318–330. <https://doi.org/10.1016/j.camwa.2013.10.001>
2. Anisimov SI, Khokhlov VA (1995) *Instabilities in Laser-matter interaction*. CRC Press, Boca Raton. ISBN 9780849386602
3. Arroyo M, Ortiz M (2006) Local maximum-entropy approximation schemes: a seamless bridge between finite elements and meshfree methods. *Int J Numer Methods Eng* 65(13):2167–2202. <https://doi.org/10.1002/nme.1534>
4. Bonacina C, Comini G, Fasano A, Primicerio M (1973) Numerical solution of phase-change problems. *Int J Heat Mass Transf* 16(10):1825–1832. [https://doi.org/10.1016/0017-9310\(73\)90202-0](https://doi.org/10.1016/0017-9310(73)90202-0)
5. Brackbill JU, Kothe DB, Zemach C (1992) A continuum method for modeling surface tension. *J Comput Phys* 100:335–354
6. Chen L, Lee JH, Chen C-F (2012) On the modeling of surface tension and its applications by the generalized interpolation material point method. *Comput Model Eng Sci* 86(3):199–223
7. Chiumenti M (1998) *Constitutive modeling and numerical analysis of thermo-mechanical phase change systems*. Ph.D. Dissertation, UPC Barcelona Tech
8. Fried I, Rheinboldt W (2014) *Numerical solution of differential equations*. Computer science and applied mathematics. Elsevier, Burlington. <http://gbv.ebib.com/patron/FullRecord.aspx?p=1901577>. ISBN 0-12-267780-3
9. Ganeriwala R, Zohdi TI (2016) A coupled discrete element-finite difference model of selective laser sintering. *Granul Matter* 18(2):21. <https://doi.org/10.1007/s10035-016-0626-0>
10. Goldak J, Chakravarti A, Bibby M (1984) A new finite element model for welding heat sources. *Metall Trans B* 15(2):299–305. <https://doi.org/10.1007/BF02667333>
11. Goldak JA, Akhlaghi M (2005) *Computational welding mechanics*. Springer, New York. ISBN 978-0387-23287-4
12. Griebel M, Knapek S, Zumbusch G (2007) *Numerical simulation in molecular dynamics: numerics, algorithms, parallelization, applications; with 63 tables*, volume 5 of SpringerLink: Springer e-Books. Springer, Berlin [u.a.], [online-ausg.] edition. ISBN 978-3-540-68095-6
13. Gross H (2005) *Fundamentals of technical optics*. Volume 1 of handbook of optical systems. Wiley, New York. ISBN 978-3-527-40377-6
14. Gu DD, Meiners W, Wissenbach K, Poprawe R (2013) Laser additive manufacturing of metallic components: materials, processes and mechanisms. *Int Mater Rev* 57(3):133–164. <https://doi.org/10.1179/1743280411Y.0000000014>
15. Gusarov AV, Yadroitsev I, Bertrand P, Smurov I (2009) Model of radiation and heat transfer in laser-powder interaction zone at selective laser melting. *J Heat Transf* 131(7):072101. <https://doi.org/10.1115/1.3109245>
16. Hecht J (2011) *Understanding lasers: an entry-level guide*, volume v.21 of IEEE press understanding science and technology series. Wiley, s.l., 3. aufl. edition. <http://gbv.ebib.com/patron/FullRecord.aspx?p=4032828>. ISBN 9780470088906
17. Hu H, Eberhard P (2016) Thermomechanically coupled conduction mode laser welding simulations using smoothed particle hydrodynamics. *Comput Part Mech* 68(2):849. <https://doi.org/10.1007/s40571-016-0140-5>
18. Hu H, Fetzner F, Berger P, Eberhard P (2016) Simulation of laser welding using advanced particle methods. *GAMM-Mitteilungen* 39(2):149–169. <https://doi.org/10.1002/gamm.201610010>
19. Hughes TJR (2000) *The finite element method: linear static and dynamic finite element analysis*. Dover, Mineola, NY, reprint edition. <http://www.loc.gov/catdir/description/dover031/00038414.html>. ISBN 0-486-41181-8
20. Khairallah SA, Anderson AT (2014) Mesoscopic simulation model of selective laser melting of stainless steel powder. *J Mater Process Technol* 214(11):2627–2636. <https://doi.org/10.1016/j.jmatprotec.2014.06.001>
21. Khairallah SA, Anderson AT, Rubenchik A, King WE (2016) Laser powder-bed fusion additive manufacturing: physics of complex melt flow and formation mechanisms of pores, spatter, and denudation zones. *Acta Mater* 108:36–45. <https://doi.org/10.1016/j.actamat.2016.02.014>
22. Ki H, Mazumder J, Mohanty PS (2002) Modeling of laser keyhole welding: part I: mathematical modeling, numerical methodology, role of recoil pressure, multiple reflections, and free surface evolution. *Metall Mater Trans A* 33(6):1817–1830. <https://doi.org/10.1007/s11661-002-0190-6>
23. Li B, Habbal F, Ortiz M (2010) Optimal transportation mesh-free approximation schemes for fluid and plastic flows. *Int J Numer Methods Eng* 83(12):1541–1579. <https://doi.org/10.1002/nme.2869>
24. Lu SCH, Pister KS (1975) Decomposition of deformation and representation of the free energy function for isotropic thermoelastic solids. *Int J Solids Struct* 11(7–8):927–934. [https://doi.org/10.1016/0020-7683\(75\)90015-3](https://doi.org/10.1016/0020-7683(75)90015-3)
25. Muhieddine M, Canot É, March R (2009) Various approaches for solving problems in heat conduction with phase change. *Int J Finite Vol* 6(1):66–85
26. Mumtaz KA, Hopkinson N (2010) Selective laser melting of thin wall parts using pulse shaping. *J Mater Process Technol* 210(2):279–287. <https://doi.org/10.1016/j.jmatprotec.2009.09.011>
27. Rosolen A, Millán D, Arroyo M (2009) On the optimum support size in meshfree methods: a variational adaptivity approach with maximum-entropy approximants. *Int J Numer Methods Eng* 139(1):868–895. <https://doi.org/10.1002/nme.2793>
28. The International Nickel Company (ed) (1968) *Mechanical and physical properties of the austenitic chromium–nickel stainless steels at elevated temperatures*, 3 edn. New York
29. Weißenfels C, Wriggers P (2018) Stabilization algorithm for the optimal transportation meshfree approximation scheme. *Comput*

- Methods Appl Mech Eng 329:421–443. <https://doi.org/10.1016/j.cma.2017.09.031>
30. Wessels H, Weißenfels C, Wriggers P (2018) Metal particle fusion analysis for additive manufacturing using the stabilized optimal transportation meshfree method. *Comput Methods Appl Mech Eng* 339:91–114. <https://doi.org/10.1016/j.cma.2018.04.042>
 31. Wriggers P (2001) *Nichtlineare finite-element-methoden*. Springer, Berlin. <https://doi.org/10.1007/978-3-642-56865-7>. ISBN 978-3-642-56865-7
 32. Wriggers P (2006) *Computational contact mechanics*. Springer, Berlin. <https://doi.org/10.1007/978-3-540-32609-0>. ISBN 978-3-540-32608-3
 33. Yan W, Smith J, Ge W, Lin F, Liu WK (2015) Multiscale modeling of electron beam and substrate interaction: a new heat source model. *Comput Mech* 56(2):265–276. <https://doi.org/10.1007/s00466-015-1170-1>
 34. Yan W, Ge W, Qian Y, Lin S, Zhou B, Wagner GJ, Lin F, Liu WK (2017) Multi-physics modeling of single/multiple-track defect mechanisms in electron beam selective melting. *Acta Materialia*. <https://doi.org/10.1016/j.actamat.2017.05.061>
 35. Zohdi TI (2006a) On the optical thickness of disordered particulate media. *Mech Mater* 38(8–10):969–981. <https://doi.org/10.1016/j.mechmat.2005.06.025>
 36. Zohdi TI (2006b) Computation of the coupled thermo-optical scattering properties of random particulate systems. *Comput Methods Appl Mech Eng* 195(41–43):5813–5830. <https://doi.org/10.1016/j.cma.2005.04.023>
 37. Zohdi TI (2010) Simulation of coupled microscale multiphysical-fields in particulate-doped dielectrics with staggered adaptive ftdtd. *Comput Methods Appl Mech Eng* 199(49–52):3250–3269. <https://doi.org/10.1016/j.cma.2010.06.032>
 38. Zohdi TI (2013) Rapid simulation of laser processing of discrete particulate materials. *Arch Comput Methods Eng* 20(4):309–325. <https://doi.org/10.1007/s11831-013-9092-6>
 39. Zohdi TI (2014) Additive particle deposition and selective laser processing—a computational manufacturing framework. *Comput Mech* 54(1):171–191. <https://doi.org/10.1007/s00466-014-1012-6>
 40. Zohdi TI (2015a) Modeling of the scattering response of particulate obscurant clouds. *Int J Eng Sci* 89:75–85. <https://doi.org/10.1016/j.ijengsci.2014.12.002>
 41. Zohdi TI (2015b) On the thermal response of a surface deposited laser-irradiated powder particle. *CIRP J Manuf Sci Technol* 10:77–83. <https://doi.org/10.1016/j.cirpj.2015.05.001>
 42. Zohdi TI (2017a) Modeling and simulation of laser processing of particulate-functionalized materials. *Arch Comput Methods Eng* 24(1):89–113. <https://doi.org/10.1007/s11831-015-9160-1>
 43. Zohdi TI (2017b) On high-frequency radiation scattering sensitivity to surface roughness in particulate media. *Comput Part Mech* 4(1):13–22. <https://doi.org/10.1007/s40571-016-0118-3>
 44. Zohdi TI (2017c) Construction of a rapid simulation design tool for thermal responses to laser-induced feature patterns. *Comput Mech* 295(7):315. <https://doi.org/10.1007/s00466-017-1503-3>
 45. Zohdi TI (2018) Laser-induced heating of dynamic particulate depositions in additive manufacturing. *Comput Methods Appl Mech Eng* 331:232–258. <https://doi.org/10.1016/j.cma.2017.11.003>
 46. Zohdi TI, Kuypers FA (2006) Modelling and rapid simulation of multiple red blood cell light scattering. *J R Soc Interface* 3(11):823–831. <https://doi.org/10.1098/rsif.2006.0139>

Publisher's Note Springer Nature remains neutral with regard to jurisdictional claims in published maps and institutional affiliations.